

RESEARCH ARTICLE

Synoptic-scale and mesoscale controls for tornadogenesis on cold fronts: A generalised measure of tornado risk and identification of synoptic types

Matthew R. Clark^{1,2,3}  | Douglas J. Parker² ¹Met Office, Exeter, UK²University of Leeds, Leeds, UK³Tornado and Storm Research Organisation (TORRO), Oxford, UK**Correspondence**M. R. Clark, Observations Development,
Met Office, FitzRoy Road, Exeter, Devon,
EX1 3PB, UK.

Email: matthew.clark@metoffice.gov.uk

Abstract

Environments of tornadic and non-tornadic narrow cold-frontal rain bands (NCFRs) are investigated using ERA-Interim reanalyses for a sample of 114 events over the United Kingdom and Ireland (44 tornadic). The results offer a practical tool for prediction of the likelihood of tornadoes in these potentially high-impact events. Of 22 analysed parameters, a bulk measure of shear vorticity, and the front-normal wind component on the cold side of the front, yield the best discrimination between event classes, showing significantly larger values in tornadic events. A generalised measure of tornado probability, $p[\text{TN}]$, is obtained using the distribution of points within the two-dimensional parameter space defined by these parameters. Synoptic situations commonly associated with tornadic NCFRs are identified and conceptual models describing the large-scale evolution are developed. Most events are associated with developing secondary cyclones (i.e., frontal waves) along trailing cold fronts ($\geq 54.5\%$), generally within west to southwesterly large-scale flow. Another significant class of event corresponds to situations where a strong mid- to upper-level jet streak cuts across the front within an amplifying large-scale flow pattern (upstream ridge building and downstream trough extension), generally within northwesterly flow (27.3%). In frontal waves, tornadoes occurred relatively early in the wave's development and just down-front of the wave centre, where rapid increases in $p[\text{TN}]$ occurred as the wave amplified. In northwesterly flow cases, tornadoes occurred along a well-defined NCFR bulge close to where the mid- to upper-level jet streak and an associated positive potential-vorticity anomaly intersected the front. Analysis of a high-tornadic subset of tornadic events (NCFRs producing ≥ 7 tornadoes) revealed an even stronger association with frontal waves (72.2% of cases), suggesting that the highest-impact events are usually associated with secondary cyclogenesis. The possible relevance of identified environmental parameters to

candidate vortex-genesis and tornadogenesis mechanisms within NCFRs and quasi-linear convective systems is discussed.

KEYWORDS

front, frontal wave, narrow cold-frontal rain band, NCFR, reanalysis, secondary cyclogenesis, tornado

1 | INTRODUCTION

Narrow cold-frontal rain bands (NCFRs) are an important source of tornadoes in the United Kingdom (UK). Mulder and Schultz (2015) found that 42% of tornadoes occurred in storms exhibiting linear morphologies in radar imagery over the period 2004–2012, of which NCFRs are a major subset. Clark and Smart (2016) found that 34.1% of tornadoes over the period 2003–2012 were associated with NCFRs specifically; this percentage increases to 48.8% when the weakest tornadoes (T0 or T1 on the International Tornado Intensity [T] Scale; Meaden, 1976a) are excluded. Furthermore, NCFRs have been responsible for many of the larger outbreaks of tornadoes in the UK (Meaden, 1976b; 1978; 1979; 1983; Elsom, 1983; 1985; Meaden and Rowe, 1985; Turner *et al.*, 1986; Apsley *et al.*, 2016). In spite of these facts, only a minority of NCFRs actually produce tornadoes. For example, of 90 NCFRs identified during the cool seasons of 2003–2010, Clark (2013) found that only 28% produced one or more tornadoes. This raises questions about how tornadic NCFRs and their environments differ from non-tornadic ones. Furthermore, questions exist about the timing of tornadogenesis, given that the tornadic phase of an NCFR tends to be short compared to its total lifetime.

Environmental parameters traditionally employed to forecast tornado risk in supercell thunderstorms and quasi-linear convective systems (QLCSs) show little skill in NCFR situations. Pre-frontal convective available potential energy (CAPE) is usually small compared to that in typical severe thunderstorm environments. Whilst statistically significant CAPE differences have been found between tornadic and non-tornadic NCFR environments (e.g. Clark, 2013), absolute differences are correspondingly small. Similarly, bulk measures of vertical wind shear cannot discriminate between tornadic and non-tornadic NCFRs, in part because strong low-level vertical wind shear is almost always present in NCFR environments, tornadic or otherwise (Gatzen, 2011; Clark, 2013). The consequent difficulty in forecasting tornado risk is compounded by the lack of conceptual models of synoptic or mesoscale situations favouring tornadogenesis in NCFRs. These issues mean that, until now, it has not been feasible

to issue forecasts of NCFR tornado risk for individual cases, even in a generalised sense (e.g. area-averaged tornado probabilities).

Analysis of the near-surface wind field has been shown to offer potential as an alternative method of predicting NCFR tornadoes. Clark and Parker (2014) (hereafter CP14) found that tornadic NCFRs usually exhibited large vertical vorticity at the surface front and a large front-normal component of flow in the cold air. Furthermore, tornadoes tended to occur immediately after, or during the latter stages of, a period of increasing vertical vorticity, leading the authors to postulate that vortex-genesis and associated tornadogenesis occurred as a result of the onset of horizontal shearing instability (HSI). Only a small sample of cases was investigated, however, leaving some doubt about the generality of the results.

In a reanalysis of the NCFR of 23 November 1981, which produced the largest tornado outbreak on record in the UK, Apsley *et al.* (2016) similarly noted the importance of vertical vorticity along the frontal boundary. They found that tornadoes occurred only where large absolute vertical vorticity coincided with positive CAPE in the immediate pre-frontal environment. As in the CP14 tornadic cases, the wind field exhibited a near-90° veer across the front, and post-frontal winds were orientated approximately normal to the NCFR. The role of temporal changes in parameters was not analysed for this case, however.

In this study, European Centre for Medium-range Weather Forecasts (ECMWF) reanalysis (ERA-Interim) data are used to examine the environments of a set of 114 fronts exhibiting NCFRs¹ over the UK and Ireland (44 tornadic). The ERA-Interim dataset contains analyses at 6-hourly intervals from January 1979 to August 2019, with a horizontal resolution of 0.75° (~80 km) and 60 vertical levels (Dee *et al.*, 2011). The purpose is two-fold. Firstly, the aim is to identify diagnostics that have skill in discriminating between tornadic and non-tornadic NCFRs, including testing whether the results of CP14 hold true

¹ A small number of the events were associated with occlusions, and so narrow frontal rain band (NFR) is a more accurate term for the analysed events than narrow cold-frontal rain band (NCFR). However, we use the latter to ensure consistency with existing nomenclature.

for a much larger set of cases. Secondly, the aim is to clarify how values of these parameters, and therefore tornado risk, relate to the synoptic- and meso-scale setting of the front, identifying specific synoptic situations in which tornadic events tend to occur. This builds on work undertaken by Gatzen (2011) and CP14; for example, Gatzen (2011) showed that severe NCFRs tend to occur at the cyclonic shear flank of strong mid-level jets, suggesting that dynamic forcing is important and that the synoptic-to meso-scale situations supportive of such events may be operationally recognisable.

The remainder of the article is structured as follows. The methodology is described in Section 2. Results are presented in Section 3. Discussion follows in Section 4 and the key messages of the article are summarised in Section 5.

2 | METHOD

2.1 | Selection of cases

NCFRs were identified using archived composite radar imagery and surface analysis charts over the period 2004–2014, using a modified version of the methodology of Trapp *et al.* (2005). This requires a quasi-linear radar echo of length at least 100 km, length at least 10 times width, and peak rainfall rates $>4 \text{ mm}\cdot\text{hr}^{-1}$. Events meeting these criteria for ≥ 2 hr, and showing at least some evidence of an NCFR for ≥ 5 hr (of any intensity or horizontal extent for the longer period) were included for analysis, in order to ensure a high probability of each analysed NCFR being present at one or more reanalysis times. Association with a surface front was sought by comparison with the surface analysis charts, so that non-frontal QLCSs could be excluded. The TORRO tornado database (www.torro.org.uk) was used to classify each event as tornadic or non-tornadic. Tornadic NCFRs were defined as those to which at least one tornado could be unambiguously attributed, based on comparison of the position of the NCFR in archived radar imagery with the location and timing of tornadoes as recorded in the TORRO database. NCFRs producing ≥ 7 tornadoes were assigned to a separate class (high-tornadic) in order to investigate whether differences exist between NCFRs producing larger outbreaks of tornadoes and those producing smaller numbers. In order to increase the sample size of high-tornadic events, the TORRO tornado database was further scrutinised to identify other instances of ≥ 7 tornadoes within a single 24 hr period between 1979 and 2003 (i.e. events that occurred within the period covered by the ERA-Interim dataset, but prior to archiving of the composite radar imagery). Non-frontal tornado outbreaks were identified and excluded by comparison of the reported

locations, dates and times of tornadoes with archived Met Office surface analysis charts; any outbreak that could not be attributed unambiguously to a frontal passage was excluded. Since these older events occurred prior to the archiving of UK composite radar imagery, it was assumed that an NCFR was present in all identified cases of frontal tornado outbreaks. In some cases, this is confirmed by radar imagery published after the event (e.g. Elsom, 1983). In others, surface analyses showed a sharp wind-shift across the front and a narrow and sharp trough collocated with the front and the line of wind-shift, features that are generally associated with NCFRs (e.g. James and Browning, 1979). Observations of these features were therefore taken to imply the presence of an NCFR in the absence of radar data. Following this procedure, nine additional high-tornadic NCFR events were identified, giving a total of 18 such events in the 1979–2014 period.

2.2 | Definition of on-front analysis points and a natural coordinate system

In the following analysis, a natural coordinate system (x' , y') is adopted in which x' is everywhere tangential to the local front and y' is everywhere normal to the local front (see inset panel in Figure 1a). Positive x' points towards lower geopotential height in the along-front direction, and positive y' points towards the cold air. The x' and y' wind components are given the notation u' and v' , respectively. The term “up-front” will be taken as the direction pointing along the front towards lower geopotential heights (i.e. the positive x' direction), and “down-front” as the direction pointing towards higher geopotential heights (i.e. the negative x' direction).

For each NCFR, analysis points were defined at regular intervals along the associated front, as depicted in Met Office surface analysis (ASXX) charts. Fronts displayed in ASXX charts are identified manually, through inspection of model data in conjunction with observations such as satellite imagery. The analyses therefore represent the best available estimate of surface frontal positions. Analysis points were defined such that the distance between adjacent points was always ≤ 150 km near the UK. For convenience, points were generally defined where the front crossed either a whole degree of latitude or longitude (whichever represented the shortest distance between points, given the orientation and latitude of the front). This methodology ensured that the separation of points was large enough for each to be located within a separate ERA-Interim grid box, but small enough for along-front variability on scales of a few hundred kilometres and larger (i.e. meso- α to synoptic scales) to be adequately resolved (Figure 1a). The first analysis point was

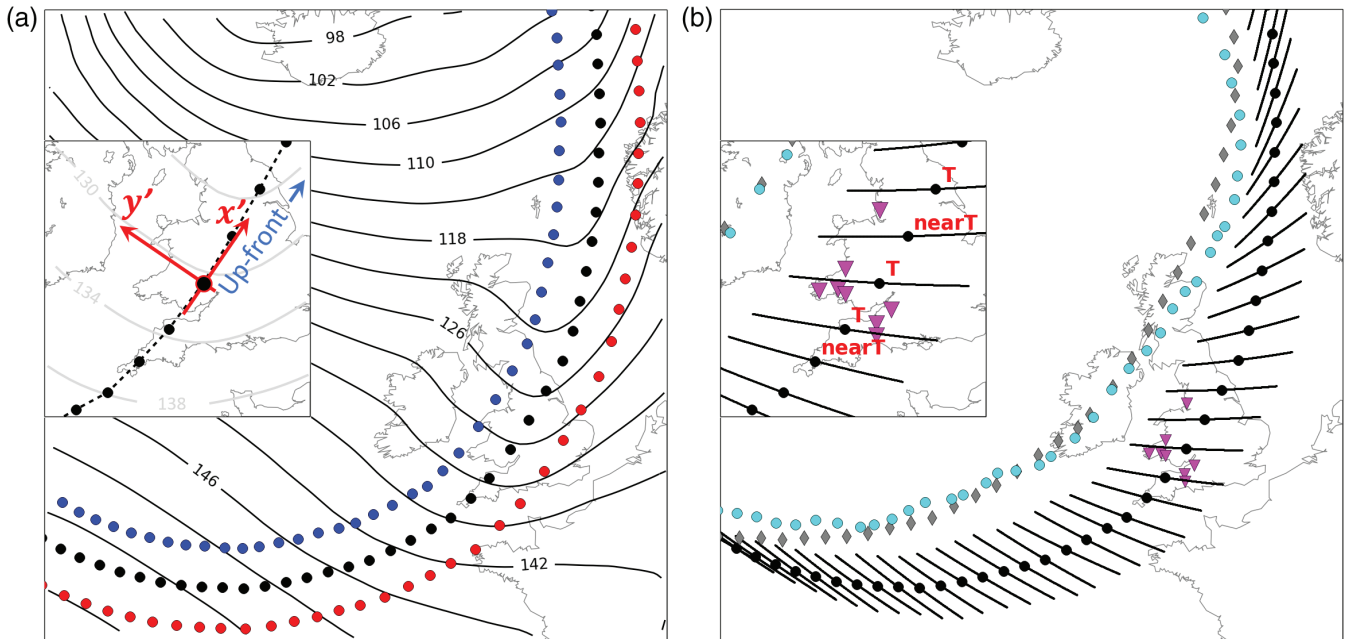


FIGURE 1 (a) On-front, warm air and cold air analysis points (black, red and blue dots, respectively) at 0000 UTC 28 December 2004, overlaid on 850 hPa geopotential height (black contours at 4 DAM intervals). Inset panel illustrates the natural coordinate system used to evaluate cross-front and along-front components. (b) Plus/minus 3 hr analysis point trajectories (black lines), derived frontal positions at previous analysis time (cyan dots) and on-front analysis points at previous analysis time (grey diamonds), where the previous analysis time is 1800 UTC 27 December 2004. Inset panel gives an expanded view of the tornadic part of the front over the UK. Tornado report locations are shown by magenta inverted triangles, with tornado classification of adjacent analysis points annotated "T" and "nearT" for tornadic and near-tornadic points, respectively

defined as the location along the front closest to the parent low-pressure centre, with subsequent points defined further down-front. The final analysis point was defined as the trailing end of the front as shown in the analysis chart, or the point at which the front extended out of the analysis domain, if applicable. Where fronts exhibited large curvature, the spacing between analysis points was reduced in order to capture the shape of the front adequately. For practical reasons, the along-front spacing was increased to ~ 250 km along the trailing portion of cold fronts at a large distance ($> \sim 1,500$ km) from the UK, if the front extended to such distances. Where a frontal wave existed that was sufficiently developed for an associated warm-front–cold-front pair to be analysed, the first analysis point was taken to be the apex of the frontal wave (i.e. the meeting point of the warm-front–cold-front pair).

In order to evaluate temporal trends, analysis points were similarly defined using ASXX charts over the period beginning 12 hr prior to the first radar detection of the NCFR and ending when the NCFR and associated front had entirely cleared the UK and Ireland. For NCFRs decaying *in situ*, points were defined up to 12 hr after the time of cessation of the NCFR. Using this method, 8,212 analysis points were defined at 270 analysis times, for 114 separate NCFR events (comprising 105 NCFRs with duration

≥ 5 hr in the 2004–2014 climatology period, and the nine additional high-tornadic events identified over the period 1979–2003). This equates to a mean number of analysis times per event of 2.4, and a mean number of on-front points per event, per analysis time, of 30.4.

2.3 | Definition of cold- and warm-air analysis points and calculation of derived parameters

For each identified event and analysis time, parameter fields were obtained from the ECMWF ERA-Interim reanalysis dataset. Parameters selected for analysis fall into four classes:

- Those known to be relevant to the vortex-gensis and tornadogenesis process in QLCSS, as shown by modelling studies (e.g. Trapp and Weisman, 2003).
- Those for which significant differences in parameter values have been found between tornadic and non-tornadic NCFR environments (e.g. Clark, 2013; CP14).
- Those known to influence the kinematic stability of shear zones (e.g. vertical vorticity and horizontal strain, and their along- and cross-frontal components, which

may relate to the potential for the development of HSI; for example, Dritschel *et al.*, 1991).

- Those relating to frontal processes, such as the two-dimensional frontogenesis function.

In order to evaluate cross-frontal differences in parameter values, where applicable, a “bulk measures” approach was adopted. Values were analysed at points located on the cold and warm sides of the front, each at a front-normal distance of 150 km from the corresponding on-front analysis point (blue and red markers in Figure 1a, respectively). The local orientation of the front was calculated from the latitude and longitude differences between neighbouring on-front points. Parameter values were obtained for the cold and warm air points by taking the value at the nearest reanalysis grid point.

Bulk measures of cross-frontal shear vorticity (i.e. $-\partial u' / \partial y'$), along-front vorticity ($\partial v' / \partial x'$), cross-front confluence ($-\partial v' / \partial y'$), and along-front dilatation ($\partial u' / \partial x'$) were calculated by evaluating finite differences in the front-normal and front-parallel flow components between corresponding cold and warm air analysis points. The cross-frontal measures (as indicated by the subscript “XF”) were defined as:

$$\text{Bulk confluence} = -D_{\text{XF}} = \frac{-\Delta v'}{\Delta y'} = \frac{(v'_{\text{warm}} - v'_{\text{cold}})}{300\text{km}}, \quad (1)$$

$$\text{Bulk shear vorticity} = \xi_{\text{XF}} = \frac{-\Delta u'}{\Delta y'} = \frac{(u'_{\text{warm}} - u'_{\text{cold}})}{300\text{km}}. \quad (2)$$

The above quantities were calculated using the full, geostrophic and ageostrophic winds, so that geostrophic and ageostrophic contributions could be evaluated separately and compared. The geostrophic wind was calculated from the 850 hPa geopotential height field, and the ageostrophic wind was obtained by subtracting the geostrophic component from the total wind field. Along-front bulk gradients (as indicated by the subscript “AF”) were calculated by analysing, on each side of the front, the mean of the gradient between the given point and the adjacent points up-front and down-front, and then by taking the mean of the resulting gradients on the warm and cold sides of the front. For example, in the case of along-front dilatation:

$$\text{Dilatation}_{\text{AF}} = 0.5 \left(\frac{\Delta u'_{\text{warm}}}{\Delta x'_{\text{warm}}} + \frac{\Delta u'_{\text{cold}}}{\Delta x'_{\text{cold}}} \right). \quad (3)$$

Along-front bulk gradients were calculated only where the horizontal separation between adjacent points on each side of the front was >50 km (the spacing being variable where the front exhibited curvature), and were not

calculated at the first and last analysis points along the front at each analysis time.

Additional parameters extracted or computed include the bulk cross-front temperature difference (temperature at the warm analysis point minus that at the cold analysis point), total frontogenesis (calculated at the *on-front* analysis point, following Markowski and Richardson (2010), p. 124), cross-frontal wind veer, ratio of the wind speeds on each side of the front (i.e. wind speed at the cold point divided by that at the warm point), front-normal, forward-directed flow at the cold air point (hereafter $-v'_{\text{cold}}$), and various measures relating to the static stability and vertical wind shear analysed at the warm air points (Table 1). Parameter values were then compared for high-tornadic, tornadic and non-tornadic points, and the *t*-test was used to assess the statistical significance of differences between event classes.

2.4 | Assumptions, limitations and interpretation of the “bulk measures” approach

The bulk measures approach assumes that parameter values are relatively uniform within the cold and warm air masses, and that gradients are constrained to a narrow zone at the front (i.e. the frontal shear zone), where the width of this zone is much less than the reanalysis grid spacing. Under these assumptions, and for a given, uniform shear zone width, the magnitude of cross-front gradients within the shear zone will be dependent only on the difference in the relevant parameter values between the warm and cold air masses. An alternative, but equivalent, interpretation is that the bulk values represent a measure of the potential magnitude of the given parameter that would be realised given collapse of the frontal shear zone to some specified, uniform, narrow width, assuming the initial width of the shear zone to be less than the 300 km separation of cold and warm air points. Since the dataset analysed here consists of NCFR-bearing fronts, collapse to small cross-frontal scales (e.g. Hoskins and Bretherton, 1972; Koch and Kocin, 1991) can be assumed for most, if not all, cases. The bulk measures have the advantage of being insensitive to the substantial small-scale variability in parameter values typically observed along and within the frontal shear zone itself. Furthermore, they avoid errors arising from uncertainties in frontal position, which could be substantial if gradients were computed at the on-front analysis points. The above assumptions were tested by recalculating various bulk parameters using a range of separation distances between the warm and cold air points (not shown). Parameters of most interest in the following analysis (notably, $-v'_{\text{cold}}$ and shear vorticity)

TABLE 1 Median values of all analysed parameters, for each event class

Parameter	Median nT [375]	Median all-T [202]	Median T [100]	Median HT [102]	<i>p</i> Value nT – all-T	<i>p</i> Value nT – T	<i>p</i> Value nT – HT	<i>p</i> Value T – HT
t–6 back trajectory terminus: distance to nearest on-front point at previous analysis time (km)	58.7	59.4	54.2	68.7	0.1788	0.3144	0.2590	0.9665
Angle of front, α (degrees clockwise from north to south with cold air to the west)	32.3	23.3	19.0	27.6	<0.0001	0.0001	0.0034	0.2969
Bulk confluence ($-dv'/dy'$) ($s^{-1} \times 10^{-5}$)	0.75	1.87	1.95	1.86	<0.0001	<0.0001	<0.0001	0.5738
Bulk confluence trend ($s^{-1} \times 10^{-5} / 6$ hr)	–0.27	0.20	–0.08	0.68	0.0013	0.6229	<0.0001	0.0079
Shear vorticity ($-du'/dy'$) ($s^{-1} \times 10^{-5}$)	2.90	5.08	4.35	5.76	<0.0001	0.0001	<0.0001	0.0014
Shear vorticity trend ($s^{-1} \times 10^{-5} / 6$ hr)	0.06	1.67	1.41	1.97	<0.0001	<0.0001	0.0002	0.3705
Bulk cross-front temperature difference (K)	4.05	4.18	3.15	5.20	0.4353	<0.0001	<0.0001	<0.0001
Cross-front temperature difference trend (K / 6 hr)	–0.17	–0.56	–0.53	–0.59	0.3699	0.5481	0.3966	0.8716
Front-normal forward motion ($m \cdot s^{-1}$)	10.5	16.4	15.8	17.6	<0.0001	<0.0001	<0.0001	<0.0001
$-v'_{cold}$ (i.e. cold-air front-normal flow) ($m \cdot s^{-1}$)	11.7	19.3	17.1	21.2	<0.0001	<0.0001	<0.0001	<0.0001
$-v'_{cold}$ trend ($m \cdot s^{-1} / 6$ hr)	–0.24	1.15	0.5	2.14	<0.0001	0.0014	<0.0001	0.0128
Front-relative $-v'_{cold}$ (forward relative flow positive) ($m \cdot s^{-1}$)	1.27	2.19	0.98	3.64	0.3616	0.1322	0.0013	0.0034
Along-front dilatation (mean of du'/dx' at warm and cold air points) ($s^{-1} \times 10^{-5}$)	0.40	–0.51	–0.49	–0.51	<0.0001	<0.0001	<0.0001	0.5093
Total frontogenesis ($K \cdot m^{-1} \cdot s^{-1} \times 10^{-10}$)	3.93	7.18	4.37	10.56	<0.0001	0.9408	<0.0001	<0.0001
Total frontogenesis trend ($K \cdot m^{-1} \cdot s^{-1} \times 10^{-10} / 6$ hr)	0.22	0.61	0.48	1.38	0.4587	0.8237	0.3299	0.6050
Cross-front wind veer (degrees)	17.5	38.6	37.7	40.7	<0.0001	<0.0001	<0.0001	0.0935
Wind speed ratio (post-front / pre-front)	0.76	0.87	0.89	0.82	<0.0001	<0.0001	<0.0001	0.2600
Overall mean wind speed ($m \cdot s^{-1}$)	21.9	23.7	21.9	25.7	<0.0001	0.3352	<0.0001	0.0006
Angle between mean wind (analysed at the cold and warm air points) and front (degrees)	33.6	53.5	50.5	56.5	<0.0001	<0.0001	<0.0001	0.0260
Surface to 850 hPa lapse rate ($K \cdot km^{-1}$) at warm air point	5.48	5.48	6.26	4.70	0.1300	<0.0001	<0.0001	<0.0001
Surface to 850 hPa saturated static stability, N_s^2 ($s^{-1} \times 10^4$) at warm air point	0.67	0.70	0.30	1.13	0.7118	<0.0001	<0.0001	<0.0001
Bulk vertical u' shear 975–850 hPa ($m \cdot s^{-1}$ difference between top and bottom of layer) at warm air point	3.85	2.91	2.29	3.71	0.0572	0.0403	0.3601	0.3574
Bulk vertical $-v'$ shear 975–850 hPa ($m \cdot s^{-1}$ difference between top and bottom of layer) at warm air point	8.35	9.75	8.59	11.37	<0.0001	0.5913	<0.0001	<0.0001

Note: *p* values are derived using Student's *t*-test. *p* values indicating differences significant at the 99% level are highlighted by bold type. Figures in square brackets indicate the sample size for each event class.

were found to be relatively insensitive to the choice of separation distance.

2.5 | Calculation of analysis-point trajectories

In order to evaluate 850 hPa parameter values in a Lagrangian frame of reference, front-following analysis points were defined by computation of “pseudo-trajectories” for each on-front point, using the observed 850 hPa u' and v' wind components at each analysis time. A parcel was assumed to move along-front with the mean u' on the cold and warm sides of the front, whilst the front-normal forward motion was assumed to approximate to $-v'_{\text{cold}}$ (the latter parameters are strongly positively correlated in the analysed sample). Back trajectories were terminated at $t - 6$ hr (i.e. the previous analysis time), where t is the current analysis time. The minimum distance between the terminus of the back trajectory at $t - 6$ hr and any on-front point at the previous analysis time was then calculated. If this distance was <100 km, the corresponding on-front point at the last analysis time was taken to be the closest on-front point to the terminus of the back trajectory. Where the minimum distance was >100 km, no corresponding point was defined and parameter trends were not calculated. Figure 1b shows an example of $t - 6$ hr trajectory end points computed using this method (cyan dots) and illustrates how they compare to the actual position of the front at the previous analysis time (grey diamonds). In general, positions calculated using the back-trajectories agreed closely with the analysed frontal position at the previous analysis time; the average distance between back trajectory terminus and closest on-front point in the preceding analysis was 75 km, and 80% of back trajectory termini were located within 100 km of an on-front point. Performance tended to be poorer where the front exhibited large curvature and close to the apex of frontal waves, situations in which larger spatio-temporal variations in the wind field might reasonably be expected.

2.6 | Classification of analysis points as non-tornadic, tornadic and high-tornadic

On-front points were categorised firstly according to whether they were associated with a high-tornadic, tornadic or non-tornadic NCFR, and then, in tornadic and high-tornadic cases, based on their proximity to tornadoes. An on-front point was classified as tornadic if the point, or any part of a trajectory extending from the point over a period of ± 3 hr from analysis time (computed in the

same way as the 6 hr back trajectories described above), lay within 50 km of a tornado report (Figure 1b). A point was classified as near-tornadic if it, or any part of its trajectory, lay between 50 and 100 km from the nearest tornado report. Points at greater distances from a tornado report were classified as “non-tornadic (of tornadic)” (nT[ofT]). All points in non-tornadic events were classified as “non-tornadic” (nT). For the purposes of comparing tornadic and non-tornadic parameter values, nT(ofT) points were excluded from the sample, because parameter values at these points cannot be considered independent of the values at neighbouring tornadic or near-tornadic points.

For nT points, two additional filters were applied. The first was to remove on-front points not situated over the UK and Ireland. This was necessary because tornadoes are unlikely to be reported over sea, so the true tornado classification of non-land points must be considered unknown. For the remaining nT points, proximity of the NCFR was assessed using composite radar rainfall imagery. Although events were selected in the first place on the basis that they exhibited an NCFR, it was not uncommon for an NCFR to affect only part of the UK and Ireland, due either to its limited along-front extent or to genesis or dissipation over the region. Points with no NCFR were removed in order to avoid the undesirable comparison of non-NCFR-bearing, non-tornadic points with tornadic points (given that the presence of an NCFR is assumed to be a prerequisite for tornadoes). An NCFR was deemed present at the given analysis point if one was evident in the radar imagery at any time within ± 3 hr from analysis time, and within a radius of approximately 100 km from the analysis point or its trajectory. This filtering, and the prior definition of non-tornadic, tornadic and high-tornadic event types, resulted in three classes of analysis point, for which the distributions of the various parameter values were compared:

- *Non-tornadic*: all analysis points along NCFR-bearing, non-tornadic fronts over the UK and Ireland.
- *Tornadic*: near-tornadic and tornadic analysis points in tornadic NCFRs (irrespective of location, but in practice always over or adjacent to the UK and Ireland, since only UK and Ireland tornadoes in the TORRO tornado database were considered).
- *High-tornadic*: as for tornadic, but in high-tornadic events.

Inspection of the analysis point trajectories and the tornado classes for each tornadic case revealed two limitations of the methodology that necessitated manual removal of a number of tornadic and near-tornadic analysis points. Firstly, where the front exhibited large curvature and the tornadoes occurred before the analysis time

in question, convergence of back-trajectories sometimes resulted in an unrealistically large along-front extent of tornadic and near-tornadic points at analysis time, compared to the along-front extent of reported tornadoes. In order to address this issue, tornadic and near-tornadic points were removed where trajectories were orientated at an angle of less than 45° to the front, if another tornadic point (or its trajectory) lay closer to the reported tornadoes. Exactly 12.4% of tornadic and high-tornadic points were removed for this reason. Secondly, tornadic and near-tornadic points were excluded where the difference between the analysis time and the nearest tornado time was >3 hr and the minimum distance between the back trajectory terminus and an on-front analysis point in the preceding analysis was >100 km. This was undertaken in order to reduce the impact of potential misclassification of points as tornadic or near-tornadic where a trajectory deviated substantially from the observed movement of the front (e.g. where there were substantial differences between front-normal forward motion and $-v'_{\text{cold}}$). Exactly 10.9% of tornadic and high-tornadic points were removed for this reason.

Following this filtering, the final number of analysis points was 375 for non-tornadic, 100 for tornadic, and 102 for high-tornadic classes. The total number of separate events in each class was 70 for non-tornadic, 26 for tornadic, and 18 for high-tornadic. In agreement with previous studies (e.g. Clark, 2013), the frequency of events showed a strong seasonal cycle, with a maximum in the autumn and early winter (86% of events occurring between October and January, with no events in June or July). Exactly 85.1% of events were associated with cold fronts, 7.0% associated with occluding cold fronts (where an NCFR was present along sections of both the cold front and the occlusion, as shown in ASXX charts) and 7.9% were associated with occlusions (see Table S1 in Appendix S1). The mean number of points per individual analysis time was 2.82 for non-tornadic, 2.27 for tornadic, and 3.00 for high-tornadic. Comparison of results using the filtered and unfiltered tornadic and high-tornadic datasets (not shown) revealed stronger differences between event classes when using the filtered dataset; however, the results were qualitatively unaffected by the filtering.

2.7 | Generation of composite analyses on a rotated, translated grid

To complement the analysis of parameter values at individual on-front points, composite analyses were generated for high-tornadic, tornadic and non-tornadic NCFRs over a domain spanning approximately 27° latitude and 50° longitude. In tornadic and high-tornadic cases, the origin of

the domain was set to the tornado or mean tornado report latitude and longitude. In non-tornadic cases, the origin was set to the mean latitude and longitude of on-front analysis points over the UK and Ireland. The origin was then translated so that it always lay at $51.5^\circ\text{N } 2.0^\circ\text{W}$, and the domain rotated such that the orientation of the front, α , was equal to the mean orientation at the origin for each event class.

Composite analyses were generated by calculating the mean parameter fields in the translated, rotated domains for all events in each NCFR category. The composites include all analysis times for which at least part of the front lay over the UK or Ireland; therefore, for some events, more than one analysis time is included. A maximum of three analysis times was allowed for each event, so as not to give undue weighting to any single event. Given the large spread in shear vorticity amongst the non-tornadic cases, two vorticity sub-classes were defined, separated by a threshold shear vorticity of $4.0 \times 10^{-5} \text{ s}^{-1}$. The aim of this partitioning was to determine whether cases with high and low vorticity were associated with distinctly different synoptic situations. This methodology resulted in compositing of 31 analysis times from 18 high-tornadic events, 35 analysis times from 26 tornadic events, 64 analysis times from 43 high-vorticity non-tornadic events, and 81 analysis times from 53 low-vorticity non-tornadic events.²

3 | RESULTS

Results are presented as follows. The distribution of parameter values in tornadic and non-tornadic events is described in Section 3.1, and the generalised measure of tornado risk is defined in Section 3.2. Along-front variability, ageostrophic contributions to key parameters, and composite fields are explored in Sections 3.3 to 3.5, from which we infer the association of many tornadic events with frontal waves. This association is explored further in Section 3.6 by inspection of surface analysis charts. Conceptual models for frontal wave and non-frontal wave events are developed in Sections 3.7 and 3.8, respectively.

3.1 | Parameter value distributions for non-tornadic, tornadic and high-tornadic event classes

Significant differences (i.e. $p < 0.01$) were found between high-tornadic, tornadic and non-tornadic classes for many

²The total number of events implied by these figures (140) is higher than the actual total (114) because some non-tornadic events contributed to both high- and low-vorticity classes at different analysis times.

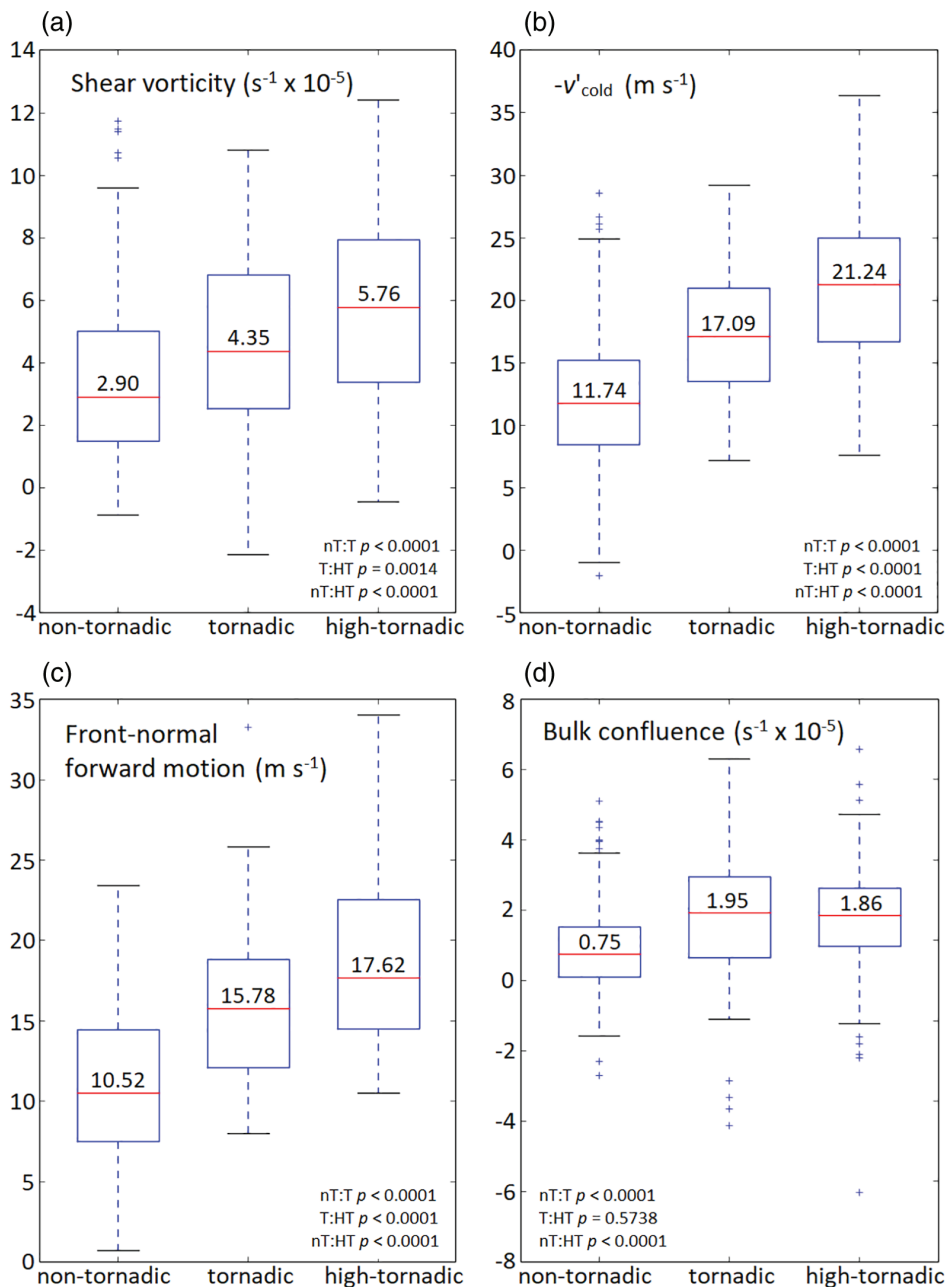


FIGURE 2 Box and whisker plots for selected parameters. (a) Shear vorticity ($s^{-1} \times 10^{-5}$); (b) $-v'_{cold}$ ($m s^{-1}$); (c) front-normal forward motion ($m s^{-1}$); (d) bulk confluence ($s^{-1} \times 10^{-5}$). Red bar and text within each box denote the median value in each case. The upper and lower edges of the box denote the upper and lower quartile values, and the whiskers extend 1.5 interquartile ranges beyond the upper and lower quartiles

of the analysed parameters (Table 1). The results for shear vorticity, wind speed ratio, and cross-front wind veer are in agreement with those of CP14, in that significantly larger values of each parameter occur in tornadic events. The fact that significant differences exist between tornadic and high-tornadic events suggests that it should be possible to distinguish between NCFR environments supporting only isolated tornadoes and those more likely to support larger outbreaks, in addition to being able to distinguish between tornadic and non-tornadic NCFR environments.

Figure 2 shows the distribution of values, by class, for parameters exhibiting statistically significant differences ($p < 0.01$) between all three event classes, and in which the

median values conform to the pattern:

$$\text{high-tornadic} > \text{tornadic} > \text{non-tornadic}.$$

These parameters are shear vorticity, front-normal forward motion and $-v'_{cold}$. Since front-normal forward motion and $-v'_{cold}$ are strongly positively correlated ($r^2 = 0.5435$), these reduce to two parameters: shear vorticity and $-v'_{cold}$. Bulk confluence is also considered further since, although median values were slightly lower in high-tornadic events than in tornadic events, differences between tornadic and non-tornadic events were amongst the largest of any analysed parameter when expressed as a percentage of the interquartile range.

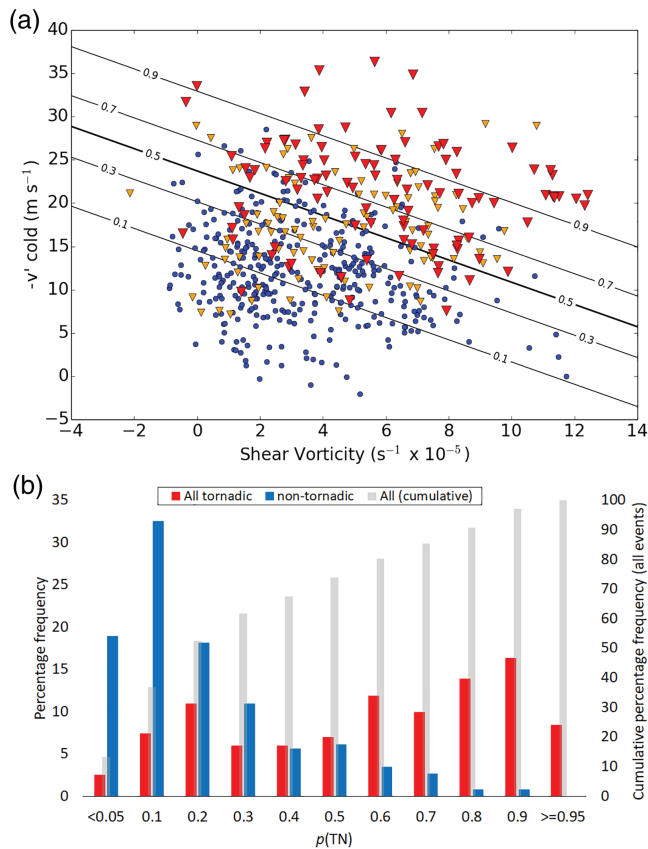


FIGURE 3 (a) Scatterplot of shear vorticity versus $-v'_{cold}$ for high-tornadic, tornadic and non-tornadic analysis points (red inverted triangles, orange inverted triangles, and blue dots, respectively). Black contours denote the probability of a point being tornadic or high-tornadic across the two-dimensional parameter space ($p[TN]$), calculated using linear discriminant analysis. (b) Histogram showing the percentage frequency of all-tornadic (i.e. tornadic plus high-tornadic) and non-tornadic events as a function of $p[TN]$. The cumulative frequency of all events, as a function of $p[TN]$, is shown by the grey bars. Values on the x-axis show the bin midpoints, except for the lowest and highest bins

3.2 | Combining shear vorticity and $-v'_{cold}$ into a single parameter to describe NCFR tornado risk

The distribution of points within the two-dimensional parameter space defined by shear vorticity and $-v'_{cold}$ is shown in Figure 3a. The probability of a point being tornadic (hereafter $p[TN]$) was calculated using linear discriminant analysis. This probability is shown by the black contours in Figure 3a. A useful partition exists between high and low $p[TN]$ environments across the parameter space, as indicated by the relatively close spacing of the probability isolines.

The frequency distribution of $p[TN]$ shows that events with small shear vorticity and $-v'_{cold}$ are considerably

more common than those with large values of both parameters (Figure 3b). For example, $\sim 50\%$ of points have $p[TN] < 0.25$, whereas only $\sim 10\%$ of points have $p[TN] > 0.75$. This is consistent with the result that only a minority of NCFRs (33.3% over the 2004–2014 period) produced one or more tornadoes. In the following sections, we show that analysis points with large shear vorticity and $-v'_{cold}$ (and therefore large $p[TN]$) tend to occur in specific synoptic situations and in well-defined locations relative to synoptic and mesoscale features along the front, such as frontal waves. We further show that these synoptic situations and along-front locations differ from those typically associated with small shear vorticity and $-v'_{cold}$.

Notwithstanding the above results, Figure 3 shows that a minority of tornadic NCFRs occur in low $p[TN]$ environments. This is illustrated in the bimodal distribution of $p[TN]$ for tornadic points in Figure 3b, with a secondary maximum in percentage frequencies at $p[TN] < 0.25$. These low $p[TN]$ tornadic cases, which represent exceptions to the rules developed in the remainder of this section, are analysed in Appendix A.

3.3 | Parameter values as a function of distance along front

Along-front variability was assessed by plotting parameter values as a function of normalised along-front distance (Figure 4). In tornadic cases, the origin was taken to be the analysis point located closest to the tornado (or to the mean position of tornadoes in cases with more than one tornado). In non-tornadic cases, the origin was taken to be the mean of analysis points located over the UK and Ireland. Points were grouped into normalised distance bins of width 100 km in order to ensure an adequate sample size. Distance bins with sample sizes < 20 were not plotted.³

Several of the parameters exhibiting significant differences between event classes in Table 1 show localised maxima near the UK in tornadic and high-tornadic classes (i.e. at normalised along-front distances near zero; Figure 4a–c). For example, $-v'_{cold}$ is maximised at distances of 200 km and 100 km in tornadic and high-tornadic classes, respectively, with strong decreases down-front (i.e. smaller $-v'_{cold}$ in the trailing section of fronts (Figure 4a)). Shear vorticity is maximised in tornadic and high-tornadic cases at the analysis point located furthest up-front (i.e. nearest to the apex of the frontal wave, where present (Figure 4d)). Statistically significant differences between

³ A threshold of 10 was used for along-front dilatation, since this parameter was calculated at fewer analysis points owing to the requirement for a minimum along-front spacing of warm-air and cold-air analysis points of 50 km, as described in Section 2.3.

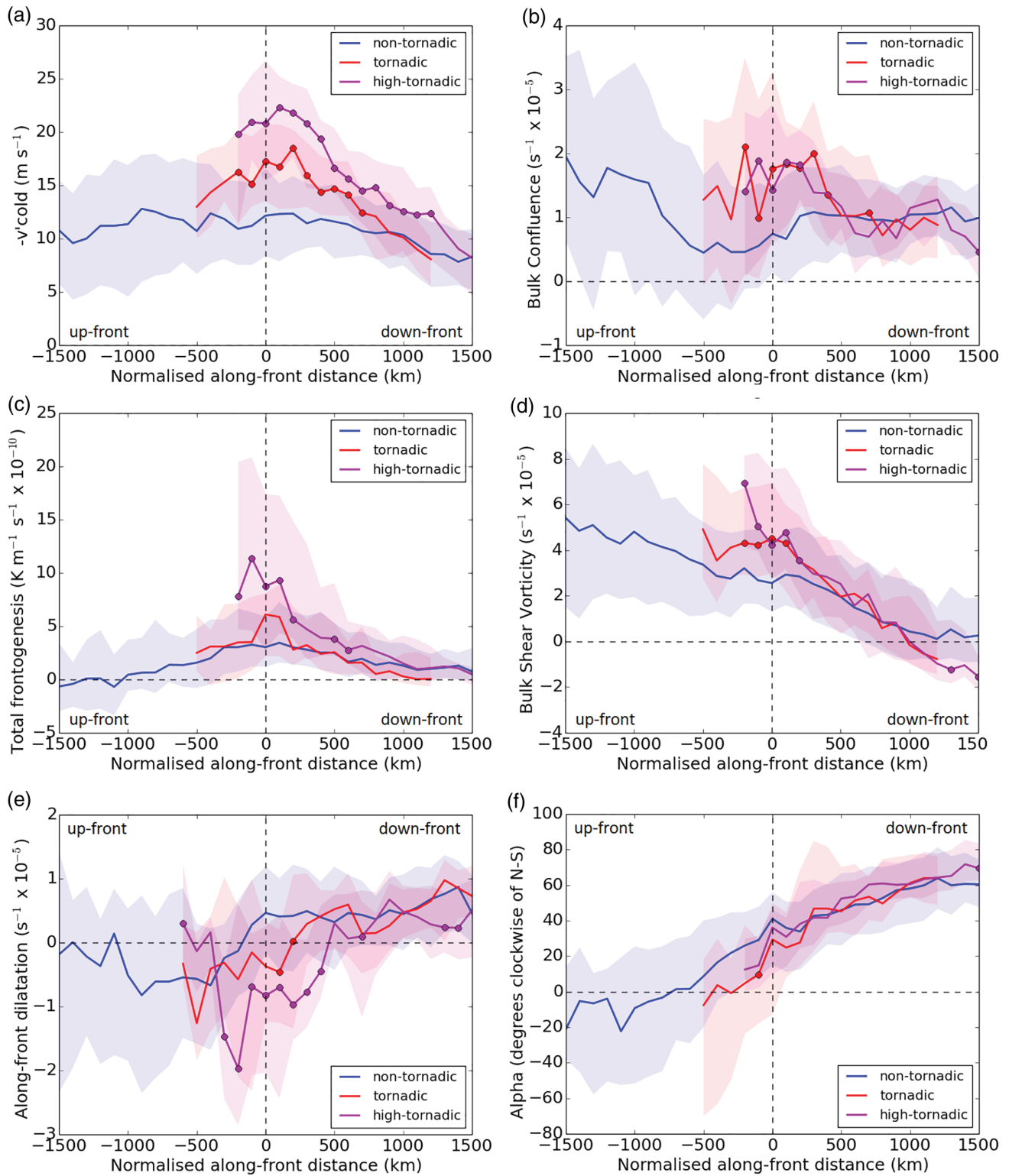
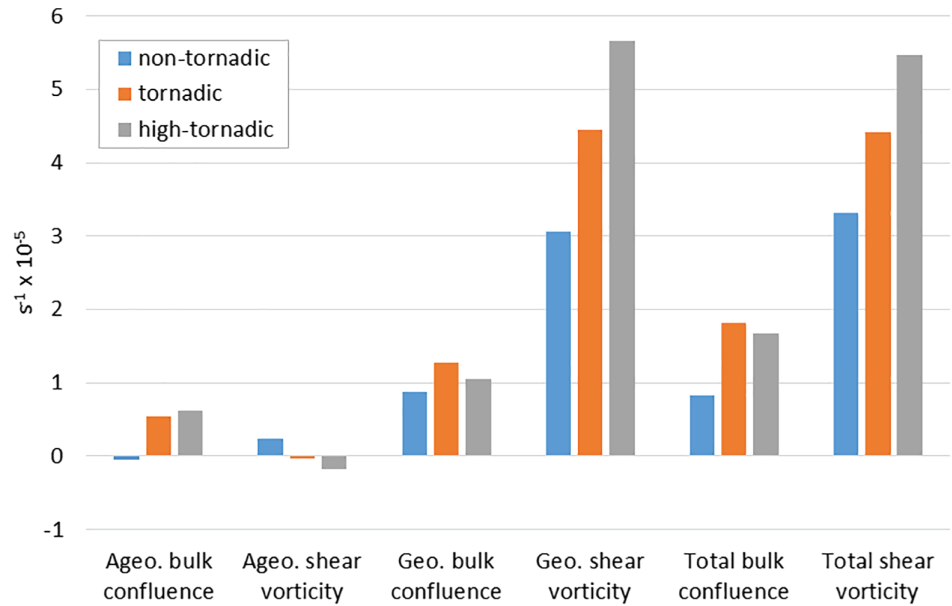


FIGURE 4 Median parameter values (bold, coloured lines) and interquartile range (shading) as a function of normalised along-front distance, where the origin is defined as the mean along-front distance of tornado reports (tornadic and high-tornadic cases), or analysis points located over the UK and Ireland (non-tornadic cases). Negative (positive) distances indicate locations up-front (down-front) of the origin. Markers are plotted at the median value where the distributions are significantly different (at the 95% level) between the non-tornadic and tornadic classes (red dots), and non-tornadic and high-tornadic classes (magenta dots). (a) $-v'_{\text{cold}}$; (b) Bulk confluence; (c) Total frontogenesis; (d) Shear vorticity; (e) Along-front dilatation; (f) Angle of front (α) (degrees clockwise of a north-south orientated front with cold air to the west)

FIGURE 5 Mean ageostrophic (left) and geostrophic (centre) contributions to the total bulk confluence and total shear vorticity (right) for each event class



event classes are generally restricted to those parts of the front located close to the UK and Ireland, with smaller differences at large along-front distances (i.e. towards the trailing end of fronts). The distance range over which differences are significant (for example, in the case of $-v'_{\text{cold}}$, -200 to 700 km in tornadic events and -200 to $1,200$ km in high-tornadic events) is on the order of the typical scale of a secondary cyclone (i.e. $\sim 1,000$ km).

In contrast to other parameters, along-front dilatation and α exhibit down-front increases in median values in all event classes. Whilst the median dilatation near the UK is negative in tornadic and high-tornadic cases, it is positive in non-tornadic cases (Figure 4e). Down-front increases in α are symptomatic of the substantial curvature exhibited by many fronts with, on average, nearly zonal orientation at the trailing ends of fronts and more meridional orientation close to the parent cyclone centre or frontal wave apex in all event classes (Figure 4f).

3.4 | Geostrophic and ageostrophic contributions to shear vorticity and confluence

Figure 5 shows the mean contributions of geostrophic, ageostrophic and total flows to the shear vorticity and bulk cross-frontal confluence for each event class, analysed at the 850 hPa level. Ageostrophic contributions to shear vorticity are small in all event classes, being only a few per cent of the total. This suggests that the front-parallel winds are largely in geostrophic balance, in agreement with previous studies (e.g. Browning and Pardoe, 1973). In contrast, whilst in non-tornadic cases ageostrophic contributions to the bulk confluence are

negligible (being only 6% of the geostrophic bulk confluence), they are positive and substantial in tornadic and high-tornadic cases (30 and 37% of the total bulk confluence, respectively). The large ageostrophic contribution is suggestive of the presence of a strong front-transverse circulation; in particular, ageostrophic confluence would be expected to occur near the leading edge of the near-ground, forward-directed branch of the circulation (e.g. Markowski and Richardson (2010), p. 124). This is consistent with the observed larger frontogenesis near to the mean tornado location in tornadic and (particularly) high-tornadic cases (Figure 4c), since the ageostrophic circulation is the atmosphere's response to the geostrophic frontogenesis.

3.5 | Composite fields

Composite fields show that all event classes are associated with synoptic patterns exhibiting generally westerly flow near the UK. At 925 hPa, the strongest winds are situated within an elongated zone on the immediate warm side of the front in all classes, which likely represents the mean position of the pre-frontal low-level jet (Figure 6). However, substantial differences exist in the structure of the frontal trough and in the strength and orientation of the post-frontal wind and pressure fields between classes. Non-tornadic (low vorticity) events exhibit a comparatively weak 925 hPa trough, with a relatively small veer in the geostrophic flow across the trough axis (Figure 6a). Non-tornadic (high vorticity) events exhibit a much sharper trough but post-frontal wind speeds are markedly weaker than in other event classes (Figure 6b).

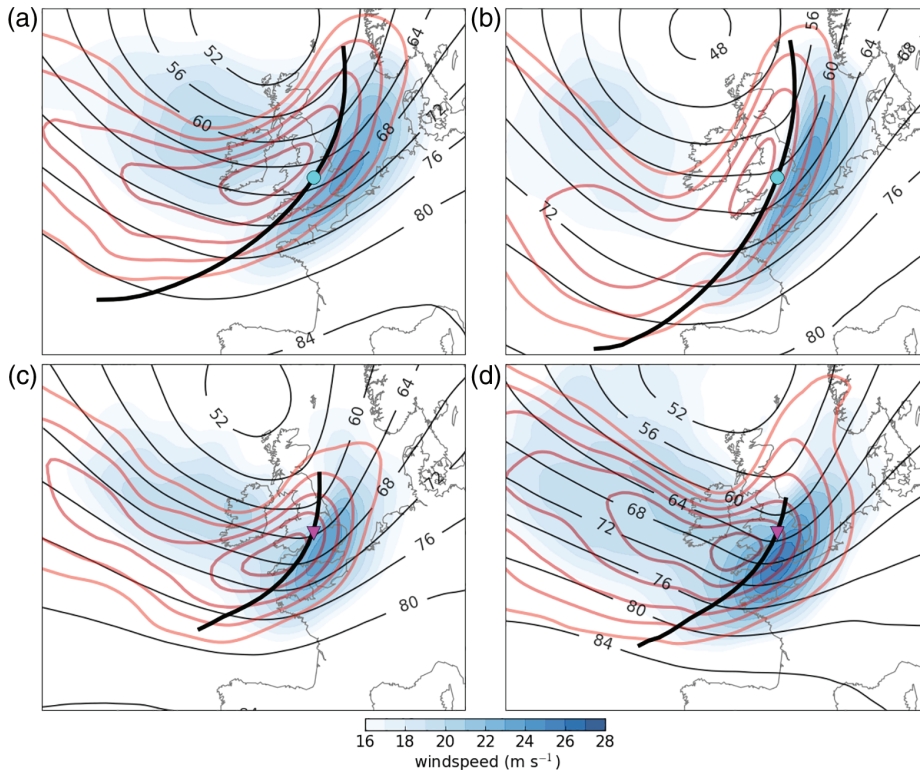


FIGURE 6 Composite plots on translated, rotated grids for all event classes: (a) low-vorticity non-tornadic; (b) high-vorticity non-tornadic; (c) tornadic; (d) high-tornadic; 925 hPa geopotential height (black contours; contour interval 4 DAM), 925 hPa wind speed (blue shading, as per the colour scale) and 300 hPa wind speed (bold, pink contours; contour interval 5 m s^{-1} starting at 30 m s^{-1}). Bold black line indicates the mean position of the surface front for each event class, plotted only where $\geq 67\%$ of events contribute an analysis point at the corresponding normalised along-front distance (where the origin is set to the mean along-front distance of tornado reports (magenta inverted triangle) or UK land analysis points (cyan circle))

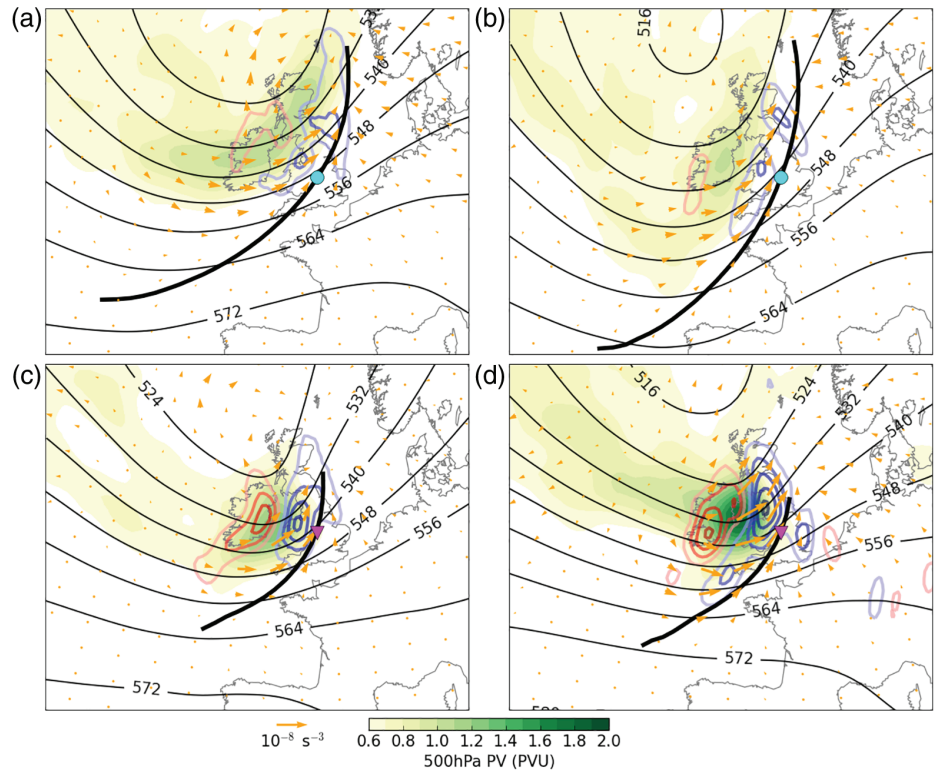
Tornadic and high-tornadic events exhibit strong pressure gradients and geostrophic wind speeds on both sides of the front, with a well-marked frontal trough, as shown by the large difference in the orientation of the 925 hPa geopotential height contours across the trough axis (Figure 6c,d). Near the UK and Ireland, post-frontal winds are orientated approximately normal to the front (i.e. west-northwesterly flow). The inequality in wind speeds between warm and cold sides of the front is much smaller than in the non-tornadic (high vorticity) events, such that these events conform closely to CP14's type A pressure and wind fields (which were likewise found to be conducive to tornadoes). The strong front-normal component of flow on the cold side of the front suggests typically fast-moving fronts. This strong flow extends many hundreds of kilometres to the rear of the front, and is therefore seen to be a characteristic of the large-scale flow field, rather than a local feature confined to the immediate post-frontal region. Compared to tornadic events, high-tornadic events exhibit slightly stronger winds and a slightly sharper frontal trough, but in general terms the fields appear similar (cf. Figure 6c,d), suggesting that the environment of high-tornadic events is essentially a stronger variant of that associated with tornadic events (as opposed to being a different type of environment entirely).

In non-tornadic (low vorticity) events (Figure 6a), the strongest 300 hPa flow is on the downwind side of the upper-level trough axis (i.e. the upper-level trough is slightly confluent). Conversely, in high-tornadic events,

the strongest flow is located on the upwind side of the trough and close to the trough axis, such that the upper-level trough is slightly diffluent (Figure 6d). In tornadic and high-tornadic events, the 300 hPa jet exit is located close to the origin (and therefore to the mean position of tornado reports), with the strongest wind speeds on the immediate cold side of the front. The jet axis crosses the surface front near the origin. In contrast, in non-tornadic events of both vorticity classes, the origin lies on the anticyclonic shear (i.e. equatorward) side of the 300 hPa jet axis, and the jet axis crosses the surface front over the North Sea, several hundred kilometres up-front of the origin. In non-tornadic (high vorticity) cases, the upper-level jet is almost parallel to the front near to the origin.

Composite fields further show that a well-defined 500 hPa potential vorticity (PV) maximum is situated on the immediate cold side of the front in all event classes (as shown by the shading in Figure 7). In non-tornadic events of both vorticity classes, the PV maximum is relatively weak and located slightly further rearward of the surface front, when compared to tornadic and high-tornadic event classes. The greater intensity and closer proximity of the PV maximum in tornadic event classes suggests greater dynamic forcing for ascent near the origin. This is confirmed by analysis of the magnitude of the vorticity advection term in the quasi-geostrophic height tendency equation (analysed at 500 hPa) and Q vectors (Sanders and Hoskins, 1990) calculated using the 700–300 hPa layer-mean wind and temperature fields

FIGURE 7 Composite plots on translated, rotated grids for all event classes: (a) low-vorticity non-tornadic; (b) high-vorticity non-tornadic; (c) tornadic; (d) high-tornadic; 500 hPa geopotential height (black contours; contour interval 8 DAM), 500 hPa PV (yellow-green shading, as per the colour scale), vorticity advection term of the quasi-geostrophic height tendency equation calculated at 500 hPa (red and blue contours indicating forcing for pressure rises and falls, respectively; contour interval $0.5 \times 10^{-12} \text{ s}^{-3}$ with the zero contour suppressed) and Q vectors calculated using the mean temperature and wind fields over the 300–700 hPa layer (orange arrows). Composite frontal positions are shown by bold black lines, as described for Figure 6



(shown by bold, red–blue contours and arrows, respectively, in Figure 7). Composites for all event classes exhibit forcing couplets close to the UK and Ireland, comprising forcing for height falls and Q-vector convergence immediately to the rear of front, and forcing for height rises and Q-vector divergence further rearward of the front. However, the forcing couplets are considerably stronger in tornadic and high-tornadic events than they are in non-tornadic events of both classes, with the strongest couplets in high-tornadic events. In the high-tornadic events, the maximum forcing for height rises corresponds closely to a region of slight anticyclonic curvature in the 925 hPa geopotential height contours over and just southeast of Ireland (cf. Figures 6d and 7d). This correspondence suggests localised large height rises (and associated additional veering of the geostrophic wind in the region between the centre of height rises and the trough axis) may contribute to the overall sharpness of the frontal trough and the magnitude of shear vorticity near to the mean tornado location.

3.6 | Association of tornadic NCFRs with frontal waves

Surface analysis charts were further inspected in order to quantify the association of tornadic and high-tornadic events with frontal waves, defined here as either a distinct warm-front–cold-front pair, or an inflection point (suggestive of a diminutive frontal wave: Hewson, 2009). Frontal

waves meeting this definition were found near the UK and Ireland in 42.3% of tornadic and 72.2% of high-tornadic cases (i.e. 54.5% of events producing any number of tornadoes). Inspection of reanalysis fields at the 925 and 850 hPa levels further revealed the presence of a local maximum in relative vertical vorticity near to the reported location of tornadoes in 60.0% of tornadic and high-tornadic cases without a warm-front–cold-front pair or inflection point, suggesting the possible presence of incipient or diminutive frontal waves (Hewson, 2009). An example of the latter occurred on 3 January 2012 (Figure 8); a local maximum in 850 hPa relative vertical vorticity is evident over southeast England at 1200 UTC, where at least one tornado occurred. Radar and surface data indicated the presence of a shallow frontal wave over the area (e.g. Figures 14 and 15 of CP14), which was evidently too weak to have been included in the ASXX charts. These results suggest that up to 77.3% of tornadic and high-tornadic events may have been associated with a frontal wave of one kind or another. Frontal waves were also present in a minority of non-tornadic NCFRs; these events, and factors distinguishing between tornadic and non-tornadic waves, are discussed in Appendix B.

3.7 | A conceptual model for tornadic NCFRs associated with frontal waves

As a frontal wave amplifies, the along-front distribution of key parameters undergoes a characteristic temporal

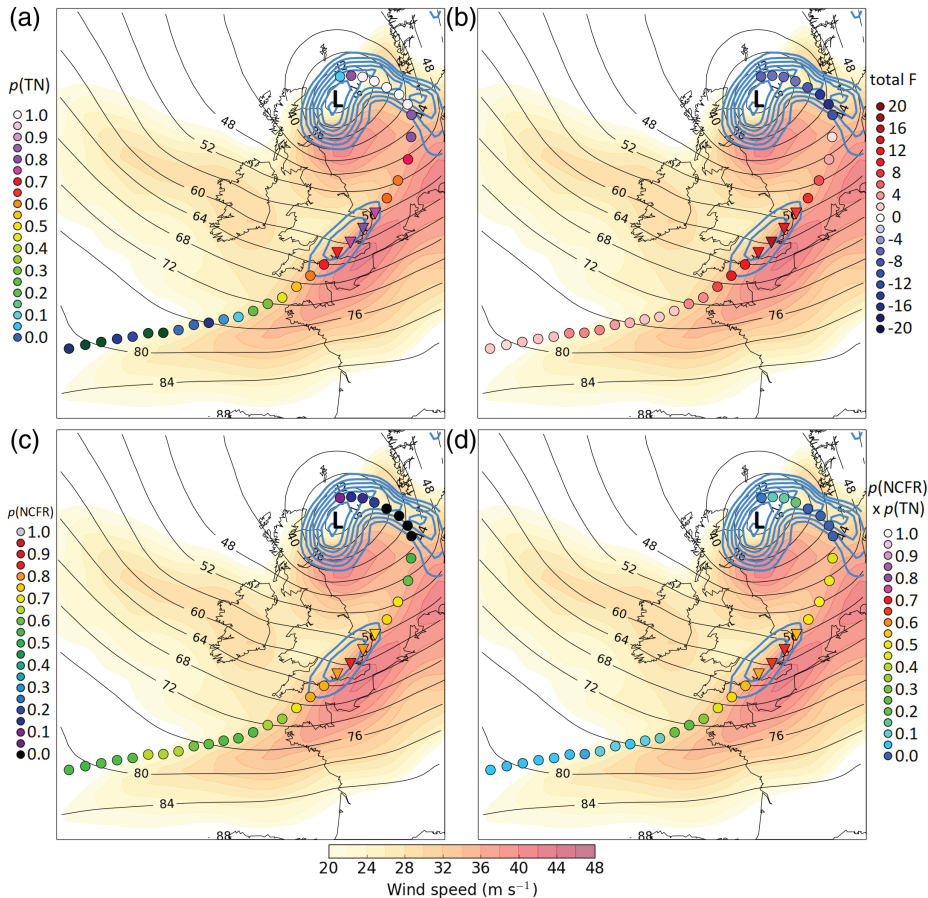


FIGURE 8 ERA-Interim fields at 1200 UTC 3 January 2012; 925 hPa geopotential height (thin black contours at 4 DAM intervals), 850 hPa wind speed (red shading; as per the colour scale) and 850 hPa relative vertical vorticity (blue contours at intervals of $0.5 \times 10^{-4} \text{ s}^{-1}$, starting at $1 \times 10^{-4} \text{ s}^{-1}$). “L” denotes the centre of the surface cyclone. Coloured circles (triangles for tornadic and near-tornadic analysis points) show along-front point values of selected parameters, according to the colour scale at the side of each panel: (a) $p[\text{TN}]$; (b) Total frontogenesis ($\text{K} \cdot \text{m}^{-1} \cdot \text{s}^{-1} \times 10^{-10}$); (c) $p(\text{NCFR})$, as based on the value of total frontogenesis (see Appendix A for details); (d) $p(\text{NCFR})$ -weighted $p[\text{TN}]$

evolution. The typical evolution is illustrated well by the high-tornadic case of 1 January 2005 (Figure 9). A frontal wave developed along a trailing cold front to the southwest of the UK early on 1 January 2005. The wave amplified rapidly as it crossed the UK between 0600 and 1800 UTC, before maturing into a relatively deep cyclone of 971 hPa over Norway by 0600 UTC 2 January 2005 (Figure 9a–c). ERA-Interim fields show a potent PV maximum approaching the trailing front from the cold air side, coming into close proximity with it and inducing the wave development just before the front reached Ireland (Figure 9d–f).

At the outset of wave development, shear vorticity and $-v'_{\text{cold}}$ are small everywhere along the front (Figure 10). However, as the wave develops, values of both parameters increase rapidly near to the wave’s centre. A maximum in shear vorticity develops at the wave centre (Figure 10b), whilst a maximum in $-v'_{\text{cold}}$ develops several hundred kilometres down-front of the wave centre, where the front begins to bulge forwards (Figure 10c). $p[\text{TN}]$, based on a combination of these two parameters, therefore increases very rapidly in the early stages of wave development, with a well-defined maximum developing just down-front of the wave centre (Figure 10a). In the analysed case, the largest value of $p[\text{TN}]$ at 0600 UTC is 0.38, increasing to 0.88 by 1200 UTC and reaching a peak of 0.98 at 1800 UTC,

by which time the front had moved out of the UK and into the North Sea. The tornadoes (star-shaped markers in Figure 10) occurred in the region of rapidly increasing $p[\text{TN}]$.

The Lagrangian evolution may be evaluated using a front-following point passing through the region with tornado reports (Figure 11; the trajectory of this point is constructed using the methodology described in Section 2.5). Tornadoes occurred near the end of the period of rapidly increasing $p[\text{TN}]$ and close to the time of maximum *front-relative* $-v'_{\text{cold}}$. The associated acceleration of this part of the front may be inferred from the position of on-front analysis points in Figure 10, the front having travelled a greater distance during the 1200–1800 UTC 1 January period than during the preceding 6 hr period.

High values of $p[\text{TN}]$ persist for ~ 6 to 12 hr after the known tornadic phase of the cold front (e.g. over southern Norway and northern Denmark in Figure 10a). Whilst it is possible that further tornadoes occurred after frontal passage over the UK, the lack of reports over north-east England and southeast Scotland suggests that the tornadic phase ended before the front crossed into the North Sea. The evolution of total frontogenesis provides a possible explanation for the cessation of tornadoes in

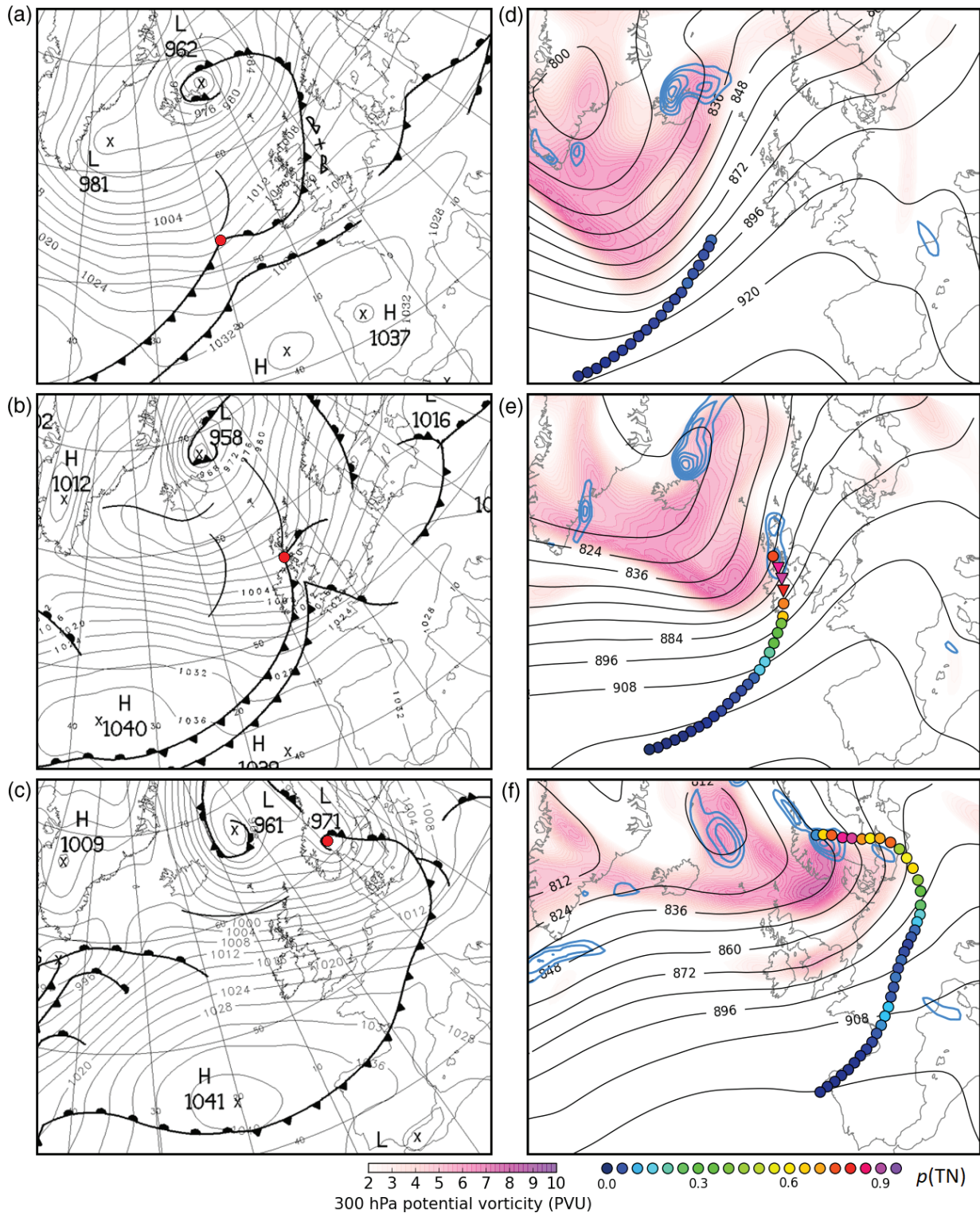


FIGURE 9 (a–c) Sequence of Met Office surface analysis charts showing mean-sea-level pressure (contour interval 4 hPa) and frontal positions. (a) 0000 UTC 1 January; (b) 1200 UTC 1 January; (c) 0600 UTC 2 January 2005. Red circles denote centre of the frontal wave at each analysis time. (d–f) ERA-Interim 300 hPa geopotential height (contour interval 12 DAM), 300 hPa PV (purple shading, as per the colour scale) and 850 hPa vertical vorticity (blue contours; contour interval $0.5 \times 10^{-4} \text{ s}^{-1}$, starting at $1 \times 10^{-4} \text{ s}^{-1}$). (d) 0000 UTC 1 January; (e) 1200 UTC 1 January; (f) 0600 UTC 2 January 2005. Circles (triangles for tornadic and near-tornadic points) in (d–f) are on-front analysis points; colour shading indicates the magnitude of $p[\text{TN}]$ at each point (as per colour scale at bottom right of the figure)

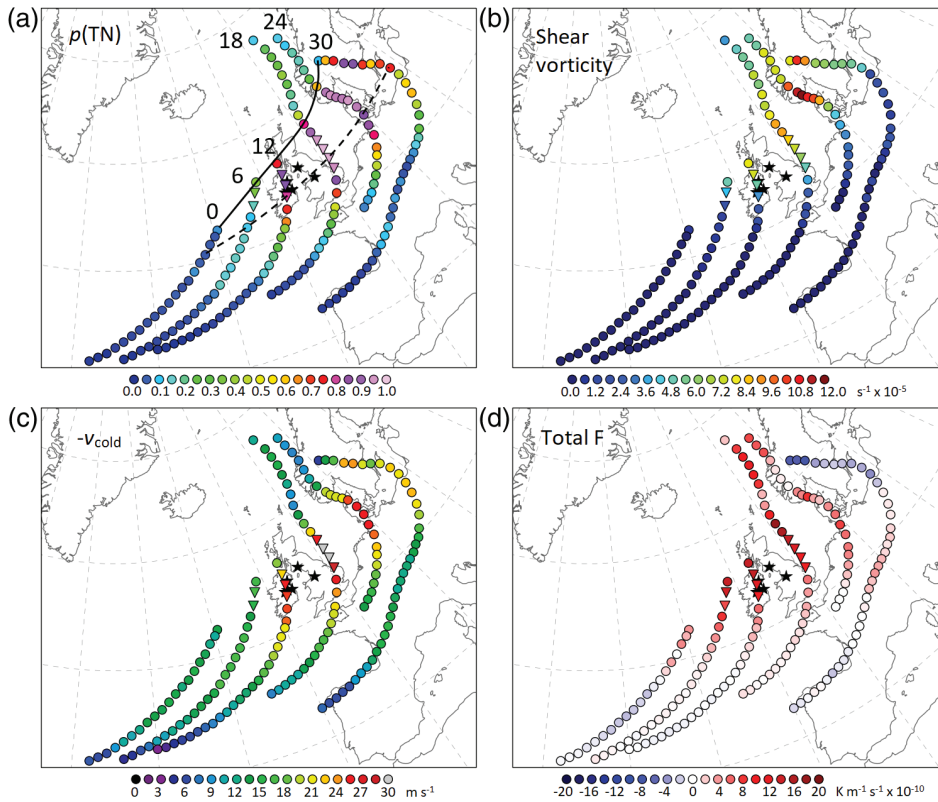


FIGURE 10 Evolution of selected parameter values for the high-tornadic case of 1 January 2005. (a) $p[TN]$; (b) shear vorticity; (c) $-v'_{cold}$; (d) total frontogenesis. On-front analysis points are shown by coloured circles (inverted triangles for tornadic and near-tornadic points), with colour shading indicating the magnitude of the corresponding parameter (as per colour scale below each panel). Black star symbols are tornado reports. Solid and dashed black lines in (a) denote, respectively, the track of the frontal wave centre and the track of a Lagrangian analysis point passing through the region of tornado reports. Figures in (a) denote the analysis time in hours after 0000 UTC 1 January 2005

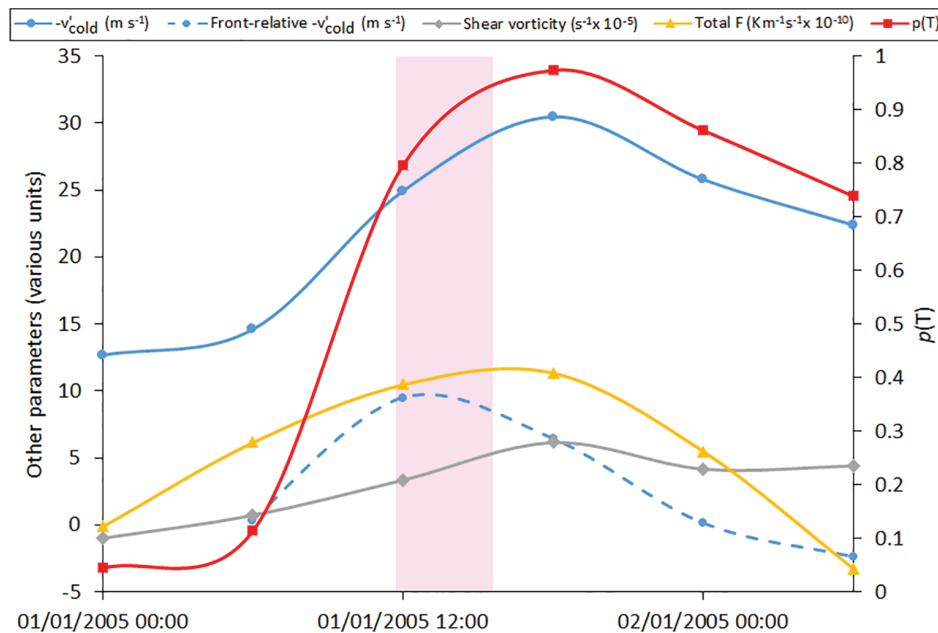


FIGURE 11 Time series of selected parameter values for a Lagrangian point passing through the region of tornado reports on 1 January 2005 (the trajectory of this point is shown by the dashed line in Figure 10a). Magenta shading denotes the tornadic phase of the event

spite of continuing high $p[TN]$; after peaking near the wave centre early in the wave’s development, frontogenesis begins to decrease, eventually becoming negative in the high $p[TN]$ region, just down-front of the wave centre (e.g. over Scandinavia in Figure 10d). Of the eight tornadic and high-tornadic cases falling most obviously into the frontal wave type, as described for the 1 January 2005 case, seven exhibited a similar transition from

frontogenesis to frontolysis in the high $p[TN]$ region as the wave matured, with seven exhibiting an associated transition from positive to negative bulk confluence in the same region. This evolution is consistent with frontal fracture in the Shapiro–Keyser cyclone life-cycle model (Shapiro and Keyser, 1990), and likely explains the oft-observed dissipation of the NCFR just down-front of the wave centre as the wave begins to mature. Whilst the NCFR tends to persist

longer along the trailing part of the front, where frontogenesis generally remains positive, $p[\text{TN}]$ is generally low in this region. Transition from frontogenetic to frontolytic flow in the otherwise tornado-favourable region just down-front of the wave centre may therefore signify the end of the period favourable for tornadoes in cases following the frontal wave conceptual model.

3.8 | A conceptual model for tornadic NCFRs not associated with frontal waves

Further analysis of the ASXX charts and ERA-Interim fields for tornadic and high-tornadic events without a frontal wave shows that many of these events occur within a synoptic regime characterised by large-scale amplification, with ridge building upstream of the UK and trough extension immediately downstream. Exactly 75.0% of non-wave cases exhibited strong curvature of the front near to the location of the tornadoes (convex on the warm side). The along-front distribution of shear vorticity and $-v'_{\text{cold}}$ along this “frontal bulge” is similar to that found along the meso- α -scale bulge down-front of the secondary cyclone in frontal wave cases, with tornadoes occurring close to the associated $p[\text{TN}]$ maximum in both types of event.

ERA-Interim wind fields show that frontal bulges in non-wave cases are associated with a discrete and often intensifying wind maximum between 925 and 300 hPa. Winds are orientated at a large angle to the front and point towards the warm air. At upper levels, the wind maximum comprises a well-defined jet streak embedded within the broader jet stream. The centre of the jet streak is typically located on the immediate cold side of the surface front, but strong flow also extends over the surface front. In 70.0% of cases without frontal waves or inflections (i.e. 31.8% of all tornadic and high-tornadic events), the tornadoes occurred underneath, or on the immediate cyclonic shear side of this jet streak (in agreement with the results of Gatzen (2011) and Clark (2013)).

Exactly 60.0% of the non-frontal-wave tornadic and high-tornadic events (27.3% of all tornadic and high-tornadic events) were associated with northerly or northwesterly flow regimes, usually with low-pressure areas moving rapidly southeast across the North Sea and a strong, amplifying ridge to the west and southwest of the UK (accordingly, these cases will be referred to as “northwesterly flow” events). Differences between this and the frontal wave scenario are illustrated by comparing composite fields for events fitting this northwesterly flow type most obviously (8 February 1984, 28 January 2004, 24 November 2005, 29 August 2010, 12 September 2012, 20 November 2013 and 25 January 2014) with those

for events fitting the frontal wave conceptual model most obviously (20 October 1981, 21 September 1982, 4 April 2004, 4 October 2004, 1 January 2005, 30 December 2006, 24 September 2007 and 17 October 2011) (Figure 12). At the analysis time closest to the tornado reports (i.e. $t + 0$ hr; Figure 12c), the mean tornado location in northwesterly flow cases is under the forward, left (i.e. cyclonic shear) flank of the jet streak and near the centre of the well-defined bulge in the surface cold front. An intense PV maximum is located at the cyclonic shear (i.e. north-east) flank of the jet streak, centred immediately behind the tornadic part of the front.

Further insight is provided by analysis of the evolution of composite fields over the period beginning 12 hr before and ending 6 hr after tornado occurrence (Figure 12a–d). Initially, the PV maximum is located to the rear of the front (Figure 12a). Over time, it gradually approaches the front, with the leading edge of $\text{PV} > 1.0$ PVU (PV units) overtaking the surface front close to the time of tornadogenesis (Figure 12c). The lower- and upper-level flow veers substantially over the same period, especially in the post-frontal region. The jet streak intensifies between $t - 12$ and $t + 0$ hr, with core speeds at 300 hPa increasing from ~ 50 to $\sim 60 \text{ m}\cdot\text{s}^{-1}$. Caution is required in the interpretation of apparent changes in intensity given that the position of features relative to the origin is likely to vary more the further the analysis time is from that at which the origin is fixed (i.e. $t + 0$), as a consequence of the variable trajectories of these features (Ayrault *et al.*, 1995). However, in this case, inspection of fields for individual events shows intensification of the jet over the period $t - 18$ to $t + 0$ hr in four of the seven cases, with subsequent weakening of the jet in the 6 hr following tornadogenesis in six of the seven cases. The substantial veering and slight strengthening of the 925 hPa flow field near the front over the $t - 18$ to $t + 0$ hr period, associated with the large-scale amplification, results in increases in $-v'_{\text{cold}}$ near the bulging section of front during the pre-tornadic period and an acceleration of the front (increasing front-normal forward motion).

By way of comparison, composite fields for frontal wave events over the period $t - 12$ to $t + 6$ hr are shown in Figure 12e–h. The 925 hPa geopotential height field strongly resembles that in the composites for all tornadic and high-tornadic events (cf. Figure 6c,d), again demonstrating the predominance of the frontal wave scenario. Relative to the northwesterly flow cases, the PV maximum at $t + 0$ is slightly weaker and located slightly further rearward of the surface front. However, in common with northwesterly flow cases, the PV maximum intensifies in the ~ 12 hr prior to tornadogenesis (cf. Figure 12e,g.) The mean position of the secondary cyclone’s centre is marked by a local maximum in low-level relative vertical vorticity and, on its poleward flank, a local weakness in the

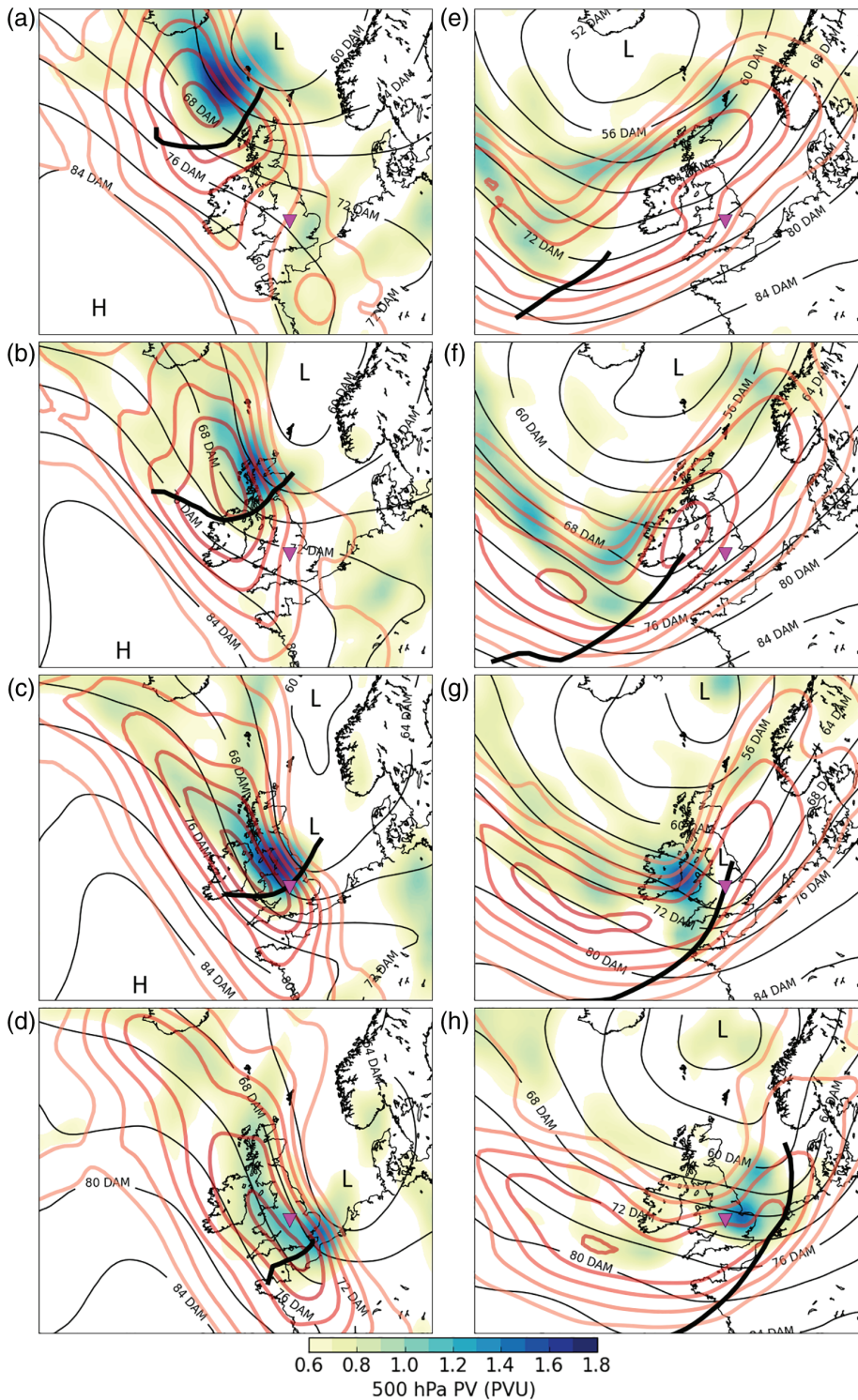


FIGURE 12 Composite fields on rotated, translated grids for (a–d) seven northwesterly flow cases and (e–h) eight frontal wave cases, six-hourly over the period $t - 12$ hr (top row) to $t + 6$ hr (bottom row), where $t + 0$ hr is the analysis time closest to the mean tornado report time. Bold black lines show mean frontal positions at each analysis time, plotted only where $\geq 67\%$ of events contribute an analysis point at the given normalised along-front distance, where zero is taken to be the mean along-front distance of tornado reports in each event. Thin black contours show 925 hPa geopotential height (contour interval 4 DAM), bold pink-red contours 300 hPa wind speed ($5 \text{ m}\cdot\text{s}^{-1}$ contour interval starting at $30 \text{ m}\cdot\text{s}^{-1}$) and green-blue shading 500 hPa PV (as per the colour scale). Rotation and translation of the domain are as described in Figure 6, whereby the mean tornado report location is set to $51.5^\circ\text{N } 2.0^\circ\text{W}$ (magenta inverted triangle in each panel)

925 hPa geopotential height gradient, centred at $t + 0$ hr over northern England, and therefore just up-front of the mean tornado location. The 300 hPa jet is slightly weaker than in the northwesterly flow composite ($\sim 50 \text{ m}\cdot\text{s}^{-1}$ near the jet core), and orientated at a shallower angle to the front. The front exhibits a bulge that is less amplified, but of longer wavelength, than that in northwesterly flow cases. The small amplification of the bulge at $t + 0$ hr likely

reflects the fact that tornadoes tend to occur at a relatively early stage in the development of the frontal wave.

4 | DISCUSSION

In this section, results are discussed in light of existing literature on cold fronts, frontal waves, and NCFRs. Firstly,

we explore the origins of large shear vorticity and $-v'_{\text{cold}}$ in frontal waves with the aid of a simple model. Secondly, we explore the variability of static stability amongst the identified event classes. Thirdly, we consider how the results relate to candidate vortex-genesis mechanisms in NCFRs and QLCSSs.

4.1 | Exploring the origins of large shear vorticity and $-v'_{\text{cold}}$ in frontal waves

In this section we use a simple model to illustrate how large values of shear vorticity and $-v'_{\text{cold}}$ come to arise within a frontal wave. In the model, the geostrophic flow is split into three components: that associated with the synoptic-scale, background pressure field, that associated with the frontal trough's pressure field, where the front bears the characteristic S-shaped inflection associated with the early stages of wave development, and that associated with the secondary cyclone's pressure field. The morphology of the frontal trough, secondary cyclone, and their associated geostrophic flow fields, are described in Appendix C.

4.1.1 | Shear vorticity

In the simple model, the background flow field is assumed to be uniform on the scale of the frontal wave and trough. Furthermore, the along-front component of flow associated with the frontal trough is assumed to be in geostrophic balance (as confirmed by Figure 5 for the set of cases analysed herein). Under these conditions, and in the absence of a secondary cyclone, large shear vorticity at the front is symptomatic of a deep frontal trough. This is because the geostrophic flow associated with the trough is of equal magnitude, but opposite sign, at given distance from the trough axis on each side of the trough (i.e. large $-du'/dy'$ across the trough axis; see Appendix C). For a fixed trough width, the magnitude of the opposing along-front flow on each side of the trough increases with increasing trough depth. However, where a secondary cyclone is present, the associated cyclonic anomaly flow field also contributes to the bulk shear vorticity, especially where the radius of curvature of the anomaly flow field is small relative to the distance across which the bulk measures are calculated, and where the anomaly flow field is strong. Given superposition of a cyclonic anomaly flow field on that associated with a frontal trough of uniform depth in the along-front direction, bulk shear vorticity will therefore be maximised near the centre of the frontal wave (Figure 13a), and will increase as the magnitude of the anomaly cyclonic wind field increases in an intensifying wave.

Although various mechanisms may contribute to the development of a frontal trough (e.g. Schultz, 2005), the feature is usually attributed to the anomalous warmth of the atmospheric column within the frontal zone, relative to that within the air masses on either side of the front (e.g. Godson, 1951). Since latent heating contributes substantially to the column-integrated warm anomaly in the frontal zone, a deep frontal trough (and therefore large geostrophic shear vorticity) may be symptomatic of large latent heating rates in strong updraughts comprising the ascending branch of a strong front-transverse ageostrophic circulation. The association of strong front-transverse circulations with frontogenesis implies that deep troughs are associated with intensifying fronts in strongly frontogenetic environments. These ideas are supported by the strong positive correlation between total frontogenesis and shear vorticity in the set of tornadic and near-tornadic analysis points in the current sample of fronts; a linear fit between $\log_e(\text{total frontogenesis})$ and shear vorticity yields an r^2 value of 0.4788 (not shown). Since the frontogenesis also tends to be maximised near to the wave centre early in the evolution of the secondary cyclone (e.g. Figure 10d), this suggests the trough is likely to be deepest (and therefore its contribution to the shear vorticity greatest) near the frontal wave centre at these early development stages. This aspect is not represented in Figure 13, since the trough is depicted as being of uniform depth across the domain.

In summary, the above considerations suggest that large bulk shear vorticity is symptomatic of fronts with deep troughs that are undergoing strong frontogenesis, especially where embedded within cyclonic anomaly flow fields associated with secondary cyclones. This explains why it tends to be maximised along the front near to the centre of actively developing secondary cyclones.

4.1.2 | Post-front normal flow, $-v'_{\text{cold}}$

In a situation with uniform background flow, and for an initially straight front, $-v'_{\text{cold}}$ is maximised down-front of the frontal wave due to the superposition of background and anomaly flow fields. Down-front of the wave centre, the anomaly flow points towards the warm air and therefore contributes positively to $-v'_{\text{cold}}$ (Figure 13b). As discussed previously, and as depicted in Figure 13, the front tends to bulge forwards on the meso- α scale in this region, owing to the controlling influence of $-v'_{\text{cold}}$ on the front-normal forward motion. On the up-front flank of the wave, the anomaly flow contributes negatively to $-v'_{\text{cold}}$ and is associated with a local minimum in front-normal forward motion. The associated along-front variations in front-normal forward motion result, over

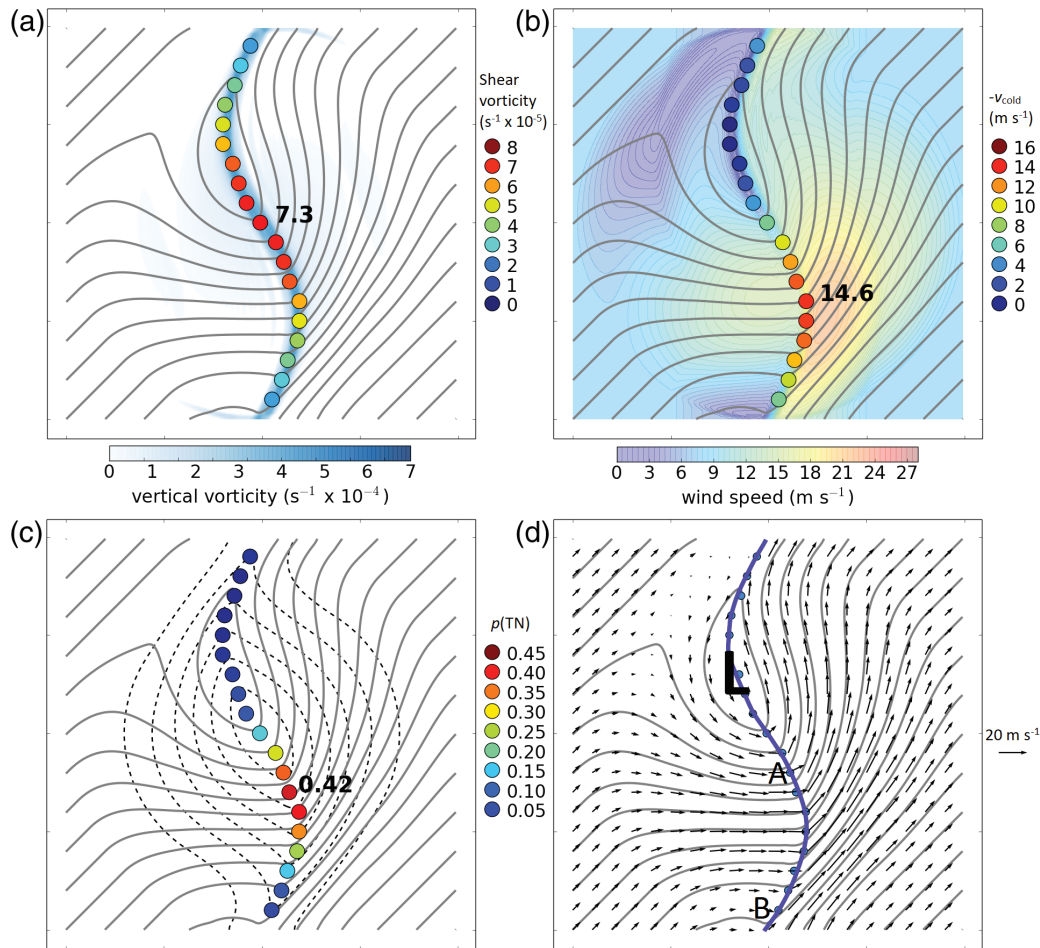


FIGURE 13 Idealised depiction of the pressure field (grey contours at 1 hPa intervals) in the early stages of frontal wave development along a trailing cold front (see Appendix C for details). Bulk measures of various parameters at on-front analysis points are shown by colour-shaded circles. (a) Vertical vorticity (shading) and shear vorticity (coloured circles); (b) total geostrophic wind speed (shading) and $-v'_{\text{cold}}$ (coloured circles); (c) pressure deficit from background (dashed contours; contour interval 1 hPa) and $p[\text{TN}]$ (coloured circles). (d) total wind field (vectors) and position of the frontal boundary (blue line). “L” denotes centre of local pressure minimum associated with the frontal wave. Letters “A” and “B” denote regions of differing trough morphology on opposite sides of the meso- α -scale frontal bulge located down-front of the wave centre (following CP14). In (a–c), the maximum value of each bulk parameter is shown in bold type adjacent to the point at which the maximum occurs

time, in development of the characteristic “S”-shaped inflection in the front.

Near the centre of the wave, the front rotates cyclonically as the wave amplifies. For an initially positively tilted front, the rotation is towards smaller positive tilt (i.e. from initial north–south (positive tilt) to northwest–southeast (neutral tilt) in the example illustrated, where the front is embedded in southwesterly large-scale flow). On the outer flanks of the S-shaped inflection, further up-front and down-front of the wave centre, the rotation is in the opposite sense; that is, the front rotates anticyclonically, and therefore becomes more positively tilted with time. This differential rotation in an initially positively tilted front results in troughs resembling CP14’s type B structure (post-frontal pressure gradients \ll pre-frontal gradients) up-front of the wave centre and on the trailing section of

front well down-front of the wave centre, and CP14’s type A structure (post-frontal gradients \approx pre-frontal gradients) immediately down-front of the wave centre (Figure 13d). In other words, the angle between the frontal trough and the background large-scale flow field has a controlling influence on the geometry of the trough (as seen in geopotential height or pressure fields), with modulation of this angle yielding the characteristic along-front variability in trough structure within and near frontal waves.

Given the initial positive tilt of the front, the cyclonic rotation near the wave centre causes the front to become orientated at a larger angle to the mean, large-scale flow (i.e. the cross-frontal component of the mean, large-scale flow increases), such that $-v'_{\text{cold}}$ will increase even in the absence of changes in the total wind field. A neutrally or negatively tilted front undergoing such rotation would

conversely experience reducing $-v'_{\text{cold}}$. However, the latter situation appears to be highly atypical of NCFR-bearing fronts; only 1.2% of points in the current sample exhibited a local orientation $\geq 90^\circ$ (i.e. perpendicular to the flow, or negatively tilted). Median values of the angle between the front and the large-scale flow field in the filtered high-tornadic, tornadic and non-tornadic datasets were 56.5° , 50.5° and 33.6° , respectively (Table 1).

Where the front possesses a strong ageostrophic transverse circulation, this circulation may also contribute to $-v'_{\text{cold}}$ immediately behind the front (i.e. in the lower branch of the circulation, where flow is directed towards the warm air). This aspect is not represented in the idealised fields in Figure 13 but, again, contributions might reasonably be expected to be maximised near the centre of the frontal wave in the early stages of wave development, where frontogenesis is maximised (as discussed in Section 3.7).

In summary, two processes contribute to the along-front maximum in geostrophic $-v'_{\text{cold}}$ near to frontal waves. Firstly, a contribution arises from the secondary cyclone's anomaly flow field. This is maximised down-front of the cyclone centre where the anomaly flow points towards the warm air. Secondly, a contribution arises from the local cyclonic turning of the front near the wave centre, in cases where the front exhibits an initial positive tilt (such that the rotation brings it closer to orthogonality to the large-scale flow). This contribution is maximised close to the wave centre. The sum of these effects is therefore maximised immediately down-front of the wave centre. Ageostrophic effects may also contribute to the total $-v'_{\text{cold}}$ where the frontogenesis is large, near the centre of the wave.

4.2 | Influence of stability and its variation with tornadic NCFR type

CP14 showed that tornadic NCFRs with relatively small vertical vorticity tend to have smaller saturated static stability (N_S^2) in the pre-frontal environment, suggesting that in these cases buoyant instability may have played a greater role in driving NCFR updraughts and, potentially, in the tornadogenesis process. In order to investigate the distribution of stability in the current set of cases, surface–850 hPa N_S^2 was calculated at the warm air analysis point for all tornadic and near-tornadic points in tornadic and high-tornadic events. Results show that 78% of tornadic and near-tornadic points have pre-frontal $N_S^2 > 0$ (i.e. moist statically stable environments). Only a very weak positive correlation was found between N_S^2 and shear vorticity ($r^2 = 0.06$; not shown); however, a stronger positive correlation was found between N_S^2 and

$\log_e(\text{total frontogenesis})$ ($r^2 = 0.20$; Figure 14a). Furthermore, points from the eight cases conforming most obviously to the frontal wave scenario (inverted triangle symbols in Figure 14) tend to be characterised by larger frontogenesis and larger stability than those from the seven cases conforming most strongly to the northwesterly flow scenario (star symbols in Figure 14). The median N_S^2 for frontal wave events is $0.95 \times 10^{-4} \text{ s}^{-2}$, which compares to $0.23 \times 10^{-4} \text{ s}^{-2}$ for northwesterly flow events. Median total frontogenesis is $14.2 \times 10^{-10} \text{ K}\cdot\text{m}^{-1}\cdot\text{s}^{-1}$ for frontal wave events and $5.4 \times 10^{-10} \text{ K}\cdot\text{m}^{-1}\cdot\text{s}^{-1}$ for northwesterly flow events, with differences significant at the 99% level ($p < 0.0001$). These differences are further illustrated by construction of smoothed kernel densities within the two-dimensional parameter space for points from each tornadic event type (colour shading in Figure 14a); the peak density in frontal wave cases is situated further towards the top right-hand side of the parameter space than it is in northwesterly flow cases. Similar stability differences between tornadic event types were found when considering the surface–850 hPa lapse rate (not shown), for which median values in frontal wave and northwesterly flow cases were 5.15 and $6.66 \text{ K}\cdot\text{km}^{-1}$, respectively, with differences significant at the 99% level ($p = 0.008$).

Differences between tornadic event types are similarly evident when plotting points in the $-v'_{\text{cold}}$ versus $\log_e(\text{total frontogenesis})$ parameter space (Figure 14b) and the $-v'_{\text{cold}}$ versus shear vorticity parameter space (Figure 14c). Frontal wave cases show significantly larger bulk vorticity and slightly smaller $-v'_{\text{cold}}$ than northwesterly flow cases, though the spread of $-v'_{\text{cold}}$ amongst northwesterly flow cases is large.

In summary, the results presented in Figure 14 suggest that tornadic NCFRs occur in a wide range of stability conditions, but that statically stable environments predominate. Where the stability is large, the frontogenesis also tends to be large. One interpretation of these results is that, whilst frontal wave development (with associated large frontogenesis and increasing shear vorticity) is generally required for tornadogenesis in statically stable environments (due to the likely involvement of kinematic instabilities within the frontal shear zone, as discussed in the following section), this requirement relaxes as the stability decreases. This is likely because convective processes (specifically, those associated with buoyant instability, rather than forced ascent) begin to play a greater role as the stability decreases. These results may be compared with the findings of Moore (1985), who demonstrated the existence of a buoyancy–shear hybrid instability for NCFRs in unstably stratified environments, as distinct from pure HSI in statically stable environments. Given the above results, we tentatively suggest that developing

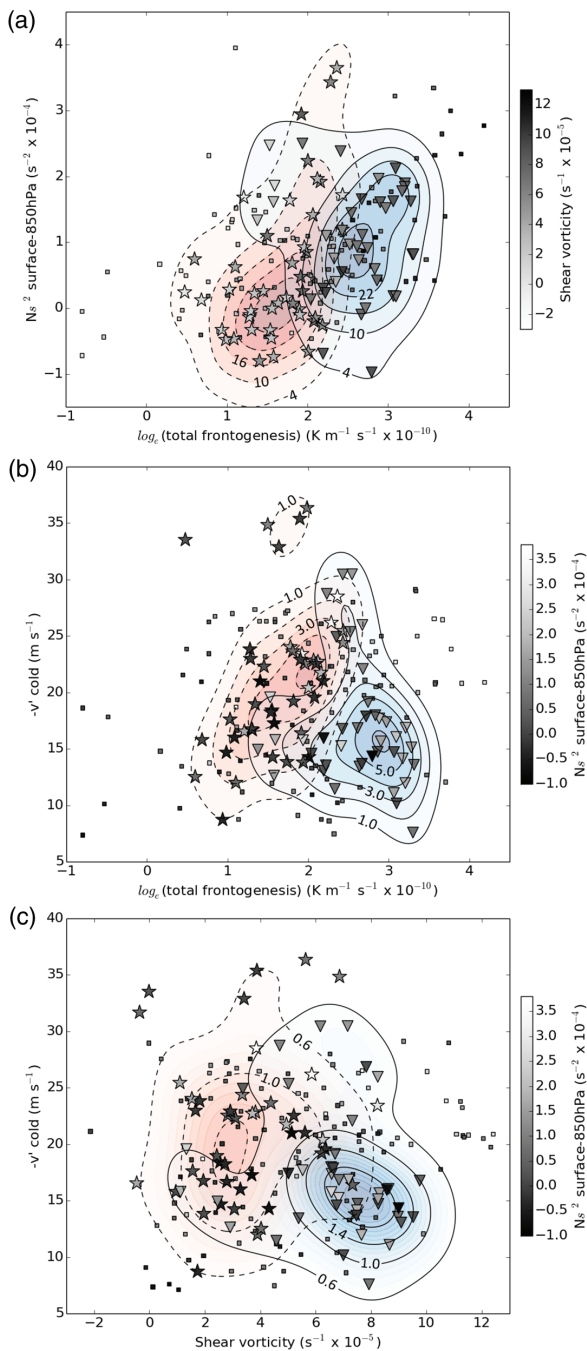


FIGURE 14 Scatterplots depicting parameter values for tornadic and near-tornadic points in tornadic and high-tornadic events. Triangles denote points belonging to the eight events conforming most closely to the frontal wave type, and stars denote points belonging to the seven events conforming most closely to the northwesterly flow type. Squares denote all other points. (a) $\log_e(\text{total frontogenesis})$ versus surface–850 hPa saturated static stability, coloured by shear vorticity; (b) $\log_e(\text{total frontogenesis})$ versus $-v'_{\text{cold}}$ coloured by surface–850 hPa saturated static stability; (c) shear vorticity versus $-v'_{\text{cold}}$ coloured by surface–850 hPa saturated static stability. Solid (dashed) contours and blue (red) shading denote the smoothed density of points, per unit area of parameter space, in the frontal wave (northwesterly flow) events

frontal waves of the type described in this study tend to produce environments supportive of pure HSI (given stable stratification in the large majority of cases), whereas northwesterly flow events produce environments that may, in at least some cases, be more supportive of the hybrid buoyancy–shear instability.

4.3 | Hypotheses concerning the relevance of the environmental parameters to candidate vortex-generation mechanisms

We now further consider how the identified environmental parameters may relate to known vortex-generation mechanisms within NCFRs, and in QLCs more generally. The discussion attempts to describe how the quantitative results obtained from the analysis of parameters can be related to various conceptual and theoretical models, and is included in the hope that it will stimulate further discussion and in order to show where future work could usefully be focussed. Some of the proposed mechanisms have been explored through analysis of high-resolution model datasets for two tornadic cases, the results of which will be presented in subsequent publications.

Radar studies show that NCFR tornadoes are often associated with mesocyclones forming along a narrow zone of strong vertical vorticity coincident with the surface front and NCFR (Carbone, 1982; 1983; Clark and Parker, 2014). Horizontal shearing instability (HSI), in which an initially uniform sheet of vertical vorticity breaks down (or “rolls up”) into discrete vertical vorticity maxima separated by areas of weaker vertical vorticity, is generally invoked as the vortex-generation mechanism (e.g. Carbone, 1983; Smart and Browning, 2009). In the non-supercell tornadogenesis mechanism described by Wakimoto and Wilson (1989) and Lee and Wilhelmson (1997), vertical stretching amplifies the vorticity to tornadic strengths when an updraught becomes collocated with the low-level vortex (albeit for shear zone vortices forming along thunderstorm outflow boundaries and other convergence zones, rather than NCFRs). On the other hand, a different mechanism – tilting of ambient horizontal vorticity – has been found to explain vortex-generation along the leading edge of QLCs in environments of large buoyant instability and large vertical wind shear (Trapp and Weisman, 2003; Weisman and Trapp, 2003; Atkins and St. Laurent, 2009). Although the dynamics of QLCs and NCFRs differ, the QLC vortices appear at least kinematically similar to NCFR mesocyclones, and so QLC vortex-generation mechanisms are also considered here.

4.3.1 | Shear vorticity

One hypothesis is that this parameter relates to the potential for HSI, and the strength of resulting vortices, along the front. Buban and Ziegler (2016) show that the rate of development and peak vertical vorticity of vortices forming as a result of HSI is directly proportional to the initial shear zone vorticity. Assuming that larger bulk shear vorticity generally equates to larger vorticity within the NCFR shear zone, this would suggest the potential for stronger and faster-developing vortices where bulk shear vorticity is larger, in the event that HSI occurs along the shear zone. Furthermore, Dritschel *et al.* (1991) show that HSI is suppressed within a vortex strip when the horizontal strain has a magnitude greater than one-quarter of the vertical vorticity within the strip. In the environment of a frontal wave, the bulk confluence (one component of the two-dimensional strain field where the axis of contraction is initially aligned with the front) generally increases near the wave centre as the wave begins to develop, consistent with the large and increasing frontogenesis along this part of the front (e.g. Figure 10d). However, as the wave continues to amplify, the bulk confluence begins to reduce again along the cyclonically turning part of the front near the wave centre (consistent with the decreasing frontogenesis along this part of the front in the latter stages of wave development, as discussed in Section 3.7). The along-front dilatation, which is the other component of the two-dimensional strain, also tends to reduce in the same region as the wave develops (as reflected by the negative median values for tornadic and high-tornadic events; Table 1). In contrast, the shear vorticity near the wave centre increases throughout the early to early-mature stages of development (e.g. as in Figure 10b, between Scotland and Norway). In other words, the shear vorticity begins to increase *relative to the strain*, such that an environment initially stable to HSI according to the Dritschel *et al.* (1991) criterion could transition to an unstable state as the frontal wave amplifies. Barotropic instability is known to be an important mechanism for the development of the frontal wave itself in some cases (e.g. Bishop and Thorpe, 1994; Dacre and Gray, 2006); our results suggest that this frontal-wave-scale instability may orchestrate the development of embedded barotropic instabilities at much smaller scales within the frontal shear zone itself. We suggest that this constitutes an important link between the sub-synoptic- and the meso- γ - to meso-scales in such cases.

Another question raised by the frequent presence of frontal waves in the analysed set of cases is why secondary cyclones are apparently more favourable for tornadoes than primary cyclones. The answer may relate to the fact that, in at least some secondary cyclones, the front has already collapsed to a narrow zone at the outset of

wave development. In such cases, an NCFR is therefore likely to be present in the tornado-favourable region in the early to early-mature developmental stages, when vorticity increases relative to the horizontal strain. In primary cyclones, the baroclinic zone is typically much wider at the outset of development, requiring a substantial period for collapse to a similarly narrow zone (e.g. Hoskins and Bretherton, 1972). Since the tornado-favourable region is collocated with the region of frontal fracture in Shapiro–Keyser type cyclones, frontal fracture in at least some primary cyclones may halt collapse before a narrow shear zone has developed, thereby preventing formation of an NCFR in the tornado-favourable region at any stage in the cyclone's development (consistent with the conceptual model of Browning and Roberts (1994), in which an NCFR is present only along the trailing cold front and back-bent front). The ability, or otherwise, for NCFRs to form or persist along the cyclonically rotating part of the front near and immediately down-front of the cyclone centre may therefore represent a key difference between cyclones of different types, and between primary and secondary cyclones in particular, in terms of their potential for hosting tornadic NCFRs.

4.3.2 | Post-front normal flow, $-v'_{\text{cold}}$

One hypothesis is that large (and in particular, increasing) $-v'_{\text{cold}}$ is favourable for intrusion of relatively dry, high-PV air into the front from the cold side. A transient period of front-relative forward flow would be expected as $-v'_{\text{cold}}$ increases, but before the front-normal forward motion has fully adjusted to the new $-v'_{\text{cold}}$, given the correlation between this parameter and front-normal forward motion, and assuming the front-normal forward motion takes some finite time to adjust to evolving $-v'_{\text{cold}}$. This period of front-relative forward flow is clearly seen in the temporal evolution of front-relative $-v'_{\text{cold}}$ at the Lagrangian point passing through the tornadic part of the front in the 1 January 2005 case (Figure 11), with tornadoes occurring close to the time of peak front-relative forward flow.⁴

Intrusions of dry air are well known to be associated with the local intensification of NCFRs and QLCSs (e.g. Johns, 1993; Browning and Reynolds, 1994; Browning and Golding, 1995; Yang and Houze, 1995; Browning *et al.*, 1997; Clough *et al.*, 2000), leading to the development of locally severe weather in some cases. The intrusion of dry air promotes evaporative cooling, which

⁴Note, however, that we cannot discount the possibility that the association between front-relative forward flow and tornadogenesis is coincidental in the analysed case.

may lead to the development of local downdraught and near-surface horizontal divergence maxima, or locally enhanced rear-to-front flow within the system. Enhanced convergence, and therefore stronger updraughts, may then occur along the convective line at the leading edge of these features. Atkins and St. Laurent (2009) demonstrate meso- γ -scale vortex-genesis through tilting of ambient horizontal vorticity on the flanks of the resulting updraught and downdraught maxima in such a scenario. An alternative possibility is that narrowing of the shear zone under the influence of the increased confluence, and associated increases in vorticity, could promote the onset of HSI should the confluence (and therefore strain) subsequently relax. In NCFRs, the enhanced cross-frontal temperature differences and increased confluence would both act to enhance frontogenesis, which could lead to local intensification of the ageostrophic front-transverse flow, with associated further increases in $-v'_{\text{cold}}$. In some cases this and other processes result in the surface front locally acquiring a density-current-like structure (e.g. Carbone, 1982; Koch and Kocin, 1991; Browning *et al.*, 1997).

An alternative hypothesis as to the relevance of $-v'_{\text{cold}}$ (and therefore the front-normal forward motion) relates to the magnitude of the cross-frontal component of vertical wind shear, and its dependency on the strength of the cross-frontal geostrophic flow. Surface friction is known to increase the magnitude of the low-level vertical wind shear (e.g. Houser *et al.*, 2016; Schenkman *et al.*, 2016). Therefore, it is logical to expect the low-level cross-frontal vertical shear to be larger when the cross-frontal flow is larger, owing to friction acting on the stronger wind field ($-v'_{\text{cold}}$ is analysed here at 850 hPa, which is generally just above the friction layer). In support of this idea, wind profiler observations of a large subset of the events investigated herein (not shown) reveal a positive correlation ($r^2 = 0.1009$) between the front-normal forward motion and the cross-frontal component of vertical shear in the 0.5–1.5 km above-ground-level layer on the warm side of the front. The cross-frontal component of vertical shear is relevant to the vortex-genesis mechanism of Trapp and Weisman (2003), in which crosswise horizontal vorticity is tilted into the vertical on the flanks of local updraught or downdraught maxima within the QLCS; stronger and deeper vortices were found by Weisman and Trapp (2003) to develop in environments possessing stronger low-level vertical wind shear.

A final hypothesis as to the relevance of $-v'_{\text{cold}}$ to the production of damaging meso- γ - or miso-scale shear zone vortices in NCFRs concerns its influence on the translational velocity of these vortices. Since the frontal shear zone and embedded vortices are constrained to move

approximately with the NCFR, larger $-v'_{\text{cold}}$ (and therefore larger front-normal forward motion) will equate to greater vortex translational velocity, assuming that the along-front component of translational velocity is relatively invariant. Due to superposition of translational and rotational velocities, and for a vortex of given rotational velocity, larger peak wind speeds will occur in the faster-moving vortex where rotational and translational velocities are additive (e.g. on the southern flank of an eastward-moving cyclonic vortex: Wakimoto *et al.*, 2006; Atkins and St. Laurent, 2009; Smart and Browning, 2009; Mahale *et al.*, 2012). Therefore, for a vortex of given intensity, the damage potential may be greater when the translational velocity is greater.

5 | SUMMARY

Through analysis of a sample of 114 events, we have demonstrated that statistically significant differences exist between the environments of tornadic and non-tornadic NCFRs. In agreement with CP14, tornadic NCFRs tend to occur in environments with larger vertical vorticity and a larger front-normal component of flow on the cold side of the front ($-v'_{\text{cold}}$). A measure of the probability of tornadoes, $p[\text{TN}]$, based upon the combined value of these parameters, has been derived. Since this measure requires knowledge only of the instantaneous wind field and the position of frontal boundaries, it could be calculated using standard operational model output, coupled with existing objective techniques for identifying the position of frontal boundaries (e.g. Hewson, 1997). The use of bulk measures, as defined in Section 2.3, should ensure that the results are robust to model resolution. In this way, a generalised measure of NCFR tornado risk may be forecastable with useful lead time. In view of the inherent unpredictability of some of the features found to have an influence on the timing and location of tornadoes, such as frontal waves, maximum benefit may be realised by applying the technique to output from ensemble models.

In order to complement the analysis of environmental parameters, synoptic situations resulting in high $p[\text{TN}]$ were explored. Two synoptic situations were found to account for the large majority (>80%) of tornadic and high-tornadic NCFRs:

- Secondary cyclogenesis (i.e. a developing frontal wave) along a trailing cold front, usually in west to southwesterly large-scale flow (at least 54.5% of all tornadic cases, and 72.2% of high-tornadic cases).
- A strong mid-level jet streak approaching and eventually cutting across the front at a large angle to it, within

an amplifying large-scale pattern, usually in northwesterly large-scale flow (at least 27.3% of all tornadic cases).

In the frontal wave scenario, tornadoes generally occur down-front of the centre of the secondary cyclone during the early stages of development, where frontogenesis is positive and $-v'_{\text{cold}}$ and shear vorticity (and therefore $p[\text{TN}]$) increase rapidly. Waves that evolve into fully fledged secondary cyclones often exhibit a transition to frontolysis down-front of the wave centre later in their life cycles; associated dissipation of the NCFR (i.e. frontal fracture) effectively ends the period of tornado risk, in spite of the continued presence of large $p[\text{TN}]$. A refined measure of tornado probability, which takes into account the magnitude and sign of frontogenesis (and therefore the likelihood of an NCFR) likely represents an improvement in this respect (as described in Appendix A). Our recommended approach in frontal wave cases is to use $p[\text{TN}]$, or the $p(\text{NCFR})$ -weighted $p[\text{TN}]$, as a first-order assessment of risk, but to view this in context of the conceptual model described in Section 3.7. The estimate of tornado probability provided by $p[\text{TN}]$ may be refined by considering the life-cycle stage of a given frontal wave at the time that it crosses the region of interest.

The second tornado-favourable situation involves a potent mid- to upper-level jet streak cutting across the front, at a large angle to the front. Tornadoes in this situation generally occur near the axis of the jet streak, or on its immediate cyclonic shear flank, where the front exhibits marked bulging. Most events of this type occurred in northwesterly flow. Large-scale amplification, characterised by upstream ridge building and downstream trough extension, appears to be an important factor; veering and strengthening of the flow between the amplifying ridge–trough couplet facilitates the approach of mid- to upper-level disturbances originating in the cold air towards the front. Analysis of stability parameters provided some limited evidence for weaker pre-frontal stability, or greater instability, in northwesterly flow cases compared to frontal wave cases. Together with the generally weaker frontogenesis in northwesterly flow events, this suggests that, on average, convective processes may play a greater role in NCFR development and tornadogenesis in northwesterly cases than in frontal wave cases.

Although we have speculated upon the possible relevance of the identified environmental parameters to vortex-genesis in NCFRs, this aspect remains an open question. Further insight is provided by subsequent analysis of high-resolution model data for a subset of cases, including examples of frontal waves and northwesterly flow events. Results of these investigations, which will be presented in future articles, confirm and clarify the nature of the links that are suggested by the present study between

frontal shear zone vortex-genesis and the evolution of the larger-scale environment.

ACKNOWLEDGEMENTS

This study was inspired by the work of the Tornado and Storm Research Organisation (TORRO), and in particular by the early studies of G. Terence Meaden and the late Derek M. Elsom, in which the association of many cold-frontal tornado outbreaks with frontal waves was first pointed out, following several notable cases in the 1970s and 1980s. The authors are grateful to Paul Brown of TORRO for providing access to the UK tornado database, without which this study would not have been possible. We also wish to thank David Smart and two anonymous reviewers for their comments, which have led to improvements in the content and presentation of this article. Parker has been supported in part by a Royal Society Wolfson Research Merit Award (2014–2018).

ORCID

Matthew R. Clark  <https://orcid.org/0000-0002-0982-9363>

Douglas J. Parker  <https://orcid.org/0000-0003-2335-8198>

REFERENCES

- Apsley, M., Mulder, K.J. and Schultz, D.M. (2016) Reexamining the United Kingdom's greatest tornado outbreak: forecasting the limited extent of tornadoes along a cold front. *Weather and Forecasting*, 31, 853–875.
- Atkins, N.T. and St. Laurent, M. (2009) Bow echo mesovortices. Part II: Their genesis. *Monthly Weather Review*, 137, 1514–1532.
- Ayrault, F., Lalaurette, F., Joly, A. and Loo, C. (1995) North Atlantic ultra high frequency variability: an introductory survey. *Tellus*, 47A, 671–696.
- Bishop, C.H. and Thorpe, A.J. (1994) Frontal wave stability during moist deformation frontogenesis. Part II: The suppression of non-linear wave development. *Journal of the Atmospheric Sciences*, 51, 874–888.
- Brooks, H.E., Doswell, C.A.I.I. and Davies-Jones, R. (1993) Environmental helicity and the maintenance and evolution of lowlevel mesocyclones. In: *In The Tornado: Its structure, dynamics, prediction, and hazard. Geophysical Monograph Series*, Vol. 79. Washington, DC: American Geophysical Union, pp. 97–104.
- Browning, K.A. and Golding, B.W. (1995) Mesoscale aspects of a dry intrusion within a vigorous cyclone. *Quarterly Journal of the Royal Meteorological Society*, 121(523), 463–493.
- Browning, K.A. and Pardoe, C.W. (1973) Structure of low-level jet streams ahead of mid-latitude cold fronts. *Quarterly Journal of the Royal Meteorological Society*, 99(422), 619–638.
- Browning, K.A. and Reynolds, R. (1994) Diagnostic study of a narrow cold-frontal rainband and severe winds associated with a stratospheric intrusion. *Quarterly Journal of the Royal Meteorological Society*, 120(516), 235–257.

- Browning, K.A. and Roberts, N.M. (1994) Structure of a frontal cyclone. *Quarterly Journal of the Royal Meteorological Society*, 120(520), 1535–1557.
- Browning, K.A., Roberts, N.M. and Illingworth, A.J. (1997) Mesoscale analysis of the activation of a cold front during cyclogenesis. *Quarterly Journal of the Royal Meteorological Society*, 123(544), 2349–2374.
- Buban, M.S. and Ziegler, C.L. (2016) The formation of small-scale atmospheric vortices via horizontal shearing instability. *Journal of the Atmospheric Sciences*, 73, 2061–2084.
- Carbone, R.E. (1982) A severe frontal rainband. Part I: Stormwide hydrodynamic structure. *Journal of the Atmospheric Sciences*, 39, 258–279.
- Carbone, R.E. (1983) A severe frontal rainband. Part II: Tornado parent vortex circulation. *Journal of the Atmospheric Sciences*, 40, 2639–2654.
- Clark, M. and Smart, D. (2016) Supercell and non-supercell tornadoes in the United Kingdom and Ireland. In: Doe, R.K. (Ed.) *In Extreme Weather: Forty years of the Tornado and Storm Research Organisation (TORRO)*. Chichester, UK: Wiley Blackwell, pp. 31–59.
- Clark, M.R. (2012) Doppler radar observations of non-occluding, cyclic vortex genesis within a long-lived tornadic storm over southern England. *Quarterly Journal of the Royal Meteorological Society*, 138(663), 439–454.
- Clark, M.R. (2013) A provisional climatology of cool-season convective lines in the UK. *Atmospheric Research*, 123, 180–196.
- Clark, M.R. and Parker, D.J. (2014) On the mesoscale structure of surface wind and pressure fields near tornadic and nontornadic cold fronts. *Monthly Weather Review*, 142(10), 3560–3585.
- Clough, S.A., Lean, H.W., Roberts, N.M. and Forbes, R.M. (2000) Dynamical effects of ice sublimation in a frontal wave. *Quarterly Journal of the Royal Meteorological Society*, 126(568), 2405–2434.
- Dacre, H.F. and Gray, S.L. (2006) Life-cycle simulations of shallow frontal waves and the impact of deformation strain. *Quarterly Journal of the Royal Meteorological Society*, 132(620), 2171–2190.
- Dee, D.P., Uppala, S.M., Simmons, A.J., Berrisford, P., Poli, P., Kobayashi, S., Andrae, U., Balmaseda, M.A., Balsamo, G., Bauer, P., Bechtold, P., Beljaars, A.C.M., van de Berg, L., Bidlot, J., Bormann, N., Delsol, C., Dragani, R., Fuentes, M., Geer, A.J., Haimberger, L., Healy, S.B., Hersbach, H., Hólm, E.V., Isaksen, I., Kållberg, P., Köhler, M., Matricardi, M., McNally, A.P., Monge-Sanz, B.M., Morcrette, J.J., Park, B.K., Peubey, C., de Rosnay, P., Tavolato, C., Thépaut, J.-N. and Vitart, F. (2011) The ERA-Interim reanalysis: configuration and performance of the data assimilation system. *Quarterly Journal of the Royal Meteorological Society*, 137(656), 553–597.
- Dritschel, D.G., Haynes, P.H., Juckes, M.N. and Shepherd, T.G. (1991) The stability of a two-dimensional vorticity filament under uniform strain. *Journal of Fluid Mechanics*, 230, 647–665.
- Elsom, D.M. (1983) Tornado at Bicester, Oxfordshire, on 21 September 1982. *Journal of Meteorology (UK)*, 8, 141–148.
- Elsom, D.M. (1985) Tornadoes formed in association with a cold front: the example of the outbreak of 21 tornadoes on 8 February 1984. *Journal of Meteorology (UK)*, 10, 4–15.
- Feuerstein, B., Dotzek, N. and Grieser, J. (2005) Assessing a tornado climatology from global tornado intensity distributions. *Journal of Climate*, 18, 585–596.
- Gatzen, C. (2011) A 10-year climatology of cold-season narrow cold-frontal rainbands in Germany. *Atmospheric Research*, 100, 366–370.
- Godson, W.L. (1951) Synoptic properties of frontal surfaces. *Quarterly Journal of the Royal Meteorological Society*, 77(334), 633–653.
- Hewson, T.D. (1997) Objective identification of frontal wave cyclones. *Meteorological Applications*, 4, 311–315.
- Hewson, T.D. (2009) Diminutive frontal waves – a link between fronts and cyclones. *Journal of the Atmospheric Sciences*, 66, 116–132.
- Hoskins, B.J. and Bretherton, F.P. (1972) Atmospheric frontogenesis models: mathematical formulation and solution. *Journal of the Atmospheric Sciences*, 29, 11–37.
- Houser, J.L., Bluestein, H.B. and Snyder, J.C. (2016) A finescale radar examination of the tornadic debris signature and weak-echo reflectivity band associated with a large, violent tornado. *Monthly Weather Review*, 144, 4101–4130.
- James, P.K. and Browning, K.A. (1979) Mesoscale structure of line convection at surface cold fronts. *Quarterly Journal of the Royal Meteorological Society*, 105(444), 371–382.
- Johns, R.H. (1993) Meteorological conditions associated with bow echo development in convective storms. *Weather and Forecasting*, 8, 294–299.
- Koch, S.E. and Kocin, P.J. (1991) Frontal contraction processes leading to the formation of an intense narrow rainband. *Meteorology and Atmospheric Physics*, 46, 123–154.
- Lee, B.D. and Wilhelmson, R.B. (1997) The numerical simulation of nonsupercell tornadogenesis. Part II: Evolution of a family of tornadoes along a weak outflow boundary. *Journal of the Atmospheric Sciences*, 54, 2387–2415.
- Mahale, V.N., Brotzge, J.A. and Bluestein, H.B. (2012) An analysis of vortices embedded within a quasi-linear convective system using X-band polarimetric radar. *Weather and Forecasting*, 27, 1520–1537.
- Markowski, P. and Richardson, Y. (2010) *Mesoscale Meteorology in Midlatitudes*. Chichester, UK: Wiley Blackwell.
- Meaden, G.T. (1976a) Tornadoes in Britain: their intensities and distribution in time and space. *Journal of Meteorology (UK)*, 1, 242–251.
- Meaden, G.T. (1976b) Tornadoes of 12 January 1975 in England. *Journal of Meteorology (UK)*, 1, 187–193.
- Meaden, G.T. (1978) Tornadoes in eastern England on 3 January 1978. *Journal of Meteorology (UK)*, 3, 225–229.
- Meaden, G.T. (1979) Tornadoes on the cold front of 12 November 1978. *Journal of Meteorology (UK)*, 4, 54–55.
- Meaden, G.T. (1983) Tornadoes and severe squalls of 21 September 1982. *Journal of Meteorology (UK)*, 8, 148–151.
- Meaden, G.T. and Rowe, M.W. (1985) The great tornado outbreak of 23 November 1981 in which north Wales, central and eastern England had 105 known tornadoes in about five hours. *Journal of Meteorology (UK)*, 10, 295–300.
- Moore, G.W.K. (1985) The organization of convection in narrow cold-frontal rainbands. *Journal of the Atmospheric Sciences*, 42, 1777–1791.
- Mulder, K.J. and Schultz, D.M. (2015) Climatology, storm morphologies, and environments of tornadoes in the British Isles: 1980–2012. *Monthly Weather Review*, 143, 2224–2240.
- Sanders, F. and Hoskins, B.J. (1990) An easy method for estimation of Q-vectors from weather maps. *Weather and Forecasting*, 5, 346–353.

- Schenkman, A.D., Xue, M. and Dawson, D.T., II. (2016) The cause of internal outflow surges in a high-resolution simulation of the 8 May 2003 Oklahoma City tornadic supercell. *Journal of the Atmospheric Sciences*, 73, 353–370.
- Schultz, D.M. (2005) A review of cold fronts with prefrontal troughs and wind shifts. *Monthly Weather Review*, 133, 2449–2472.
- Shapiro, M.A. and Keyser, D. (1990) Fronts, jet streams and the tropopause. In: Newton, C.W. and Holopainen, E.O. (Eds.) *In Extratropical Cyclones, The Erik Palmén Memorial*. Boston, MA: American Meteorological Society, pp. 167–191.
- Smart, D.J. and Browning, K.A. (2009) Morphology and evolution of cold-frontal mesocyclones. *Quarterly Journal of the Royal Meteorological Society*, 135(639), 381–393.
- Trapp, R.J., Tessendorf, S.A., Godfrey, E.S. and Brooks, H.E. (2005) Tornadoes from squall lines and bow echoes. Part I: Climatological distribution. *Weather and Forecasting*, 20, 23–34.
- Trapp, R.J. and Weisman, M.L. (2003) Low-level mesovortices within squall lines and bow echoes. Part II: Their genesis and implications. *Monthly Weather Review*, 131, 2804–2823.
- Turner, S., Elsom, D.M. and Meaden, G.T. (1986) An outbreak of 31 tornadoes associated with a cold front in southern England on 20 October 1981. *Journal of Meteorology (UK)*, 11, 37–50.
- Wakimoto, R.M., Murphey, H.V., Davis, C.A. and Atkins, N.T. (2006) High winds generated by bow echoes. Part II: The relationship between the mesovortices and damaging straight-line winds. *Monthly Weather Review*, 134, 2813–2829.
- Wakimoto, R.M. and Wilson, J.W. (1989) Non-supercell tornadoes. *Monthly Weather Review*, 117, 1113–1140.
- Weisman, M.L. and Trapp, R.J. (2003) Low-level mesovortices within squall lines and bow echoes. Part I: Overview and dependence on environmental shear. *Monthly Weather Review*, 131, 2779–2803.
- Yang, M. and Houze Jr, R.A. (1995) Sensitivity of squall-line rear inflow to ice microphysics and environmental humidity. *Monthly Weather Review*, 123, 3175–3193.

SUPPORTING INFORMATION

Additional supporting information may be found online in the Supporting Information section at the end of this article.

How to cite this article: Clark MR, Parker DJ. Synoptic-scale and mesoscale controls for tornadogenesis on cold fronts: A generalised measure of tornado risk and identification of synoptic types. *QJR Meteorol Soc.* 2020;146:4195–4225. <https://doi.org/10.1002/qj.3898>

APPENDIX A

Analysis of low p [TN] tornadic NCFRs (exceptions)

As demonstrated by Brooks *et al.* (1993), analysis of “failure modes” for severe convection and related

phenomena may be as instructive as analysis of supporting factors, and for this reason we analyse, in this Appendix, exceptions to the rule that large $-v'_{\text{cold}}$ and large shear vorticity tend to favour tornadoes.

Tornadic points with low p [TN]

Manual inspection of surface analysis charts and 850 hPa geopotential height fields suggests that most tornadic points with p [TN] <0.3 arise as a result of limitations in the analysis methodology and datasets, rather than being indicative of events in genuinely low shear vorticity and/or low $-v'_{\text{cold}}$ environments. Firstly, some points are explained by the occurrence of frontal waves that were too small to be resolved on the ERA-Interim reanalysis grid. An example is the cold front of 3 November 2009. Surface meso-analyses showed a frontal wave and collocated surface meso-low with a wavelength of only a few tens of kilometres along a trailing cold front (Clark, 2012). The wind field around the meso-low is suggestive of $-v'_{\text{cold}}$ and shear vorticity locally much larger than in the reanalysis dataset. This event therefore appears to represent a special class of the frontal wave type, in which the horizontal scale of the secondary cyclone (and therefore the tornado-favourable section of the front) is unusually small. Four points (8.3% of those with p [TN] <0.3) fit into this category.

A second explanation for low p [TN] points is large along-front gradients in p [TN], which sometimes resulted in values of $-v'_{\text{cold}}$ and/or shear vorticity at the analysis point being unrepresentative of those at the tornado location. This issue is suggested by the presence of adjacent analysis points with much larger p [TN]; for example, 25.0% of points with p [TN] <0.3 were located within ± 2 points (i.e. $\pm \sim 220$ km) of a point with p [TN] ≥ 0.5 . Some of these points occurred close to the apex of frontal waves. Filtering to remove points with trajectories orientated at a shallow angle to the front, where another point lay closer to the observed tornado location (as described in Section 2.6), reduces the number of points affected by this problem, but evidently some examples remain.

A third, and related, situation in which points with low p [TN] occurs is along fronts with large curvature, especially where the tornadic or near-tornadic point in question is situated on the down-front flank of a prominent bulge in the line (such as might occur down-front of a developing secondary cyclone). Twenty-five (i.e. 52.1%) of the tornadic and near-tornadic points with p [TN] <0.3 were associated with sections of fronts exhibiting substantial curvature, of which 16 were located down-front of the centre of a prominent frontal bulge. Comparison of the actual tornado locations with the frontal bulges in these cases showed that tornadoes genuinely occurred on the

trailing flanks of the frontal bulges in only five cases. Given the typically large along-front differences in key parameter values between the up-front and down-front flanks of frontal bulges, this suggests that, in the remaining 11 cases, conditions at the given point are unlikely to have been representative of those at the actual tornado location. This issue tends to arise when the along-front scale of the frontal wave and associated frontal bulge is relatively small, or where the frontal bulge was evolving rapidly.

The remaining points with $p[\text{TN}] < 0.3$ cannot be explained by limitations of the methodology, and therefore genuinely appear to be exceptions to the rule that tornadic fronts occur in high shear vorticity and high $-v'_{\text{cold}}$ environments; 21 points (43.8% of tornadic and near-tornadic points with $p[\text{TN}] < 0.3$, and 10.4% of all tornadic and near-tornadic points) fall into this category. Most of these points were associated with events exhibiting anomalously weak wind fields, some of which occurred in the warm half of the year. For example, 5 of the 21 points were associated with the event of 29 August 2012. CP14, in their analysis of 15 events, found an anomalously unstable pre-frontal environment in the 29 August 2012 case ($N_s^2 < 0$), as estimated from pre-frontal proximity soundings. Analysis of pre-frontal N_s^2 in the current set of cases (see Section 4.2) reveals negative values for 10 of the 21 low $p[\text{TN}]$ tornadic and near-tornadic points that are not explained by limitations of the methodology, with a median N_s^2 over all 21 points of $0.00 \times 10^{-4} \text{ s}^{-1}$. This is substantially lower than the all-tornado-cases median value of $0.70 \times 10^{-4} \text{ s}^{-1}$ (Table 1), with differences significant at the 95% level. These results suggest that tornadic points in low $p[\text{TN}]$ environments that cannot be explained by limitations of the methodology represent a set of cases in which buoyant instability plays a greater role in NCFR formation and tornadogenesis, and in which kinematic parameters such as the vertical vorticity and $-v'_{\text{cold}}$ play a lesser role, than is typical for NCFR events.

Non-tornadic points with high $p[\text{TN}]$

In the unfiltered set of non-tornadic analysis points over UK and Ireland land areas (i.e. including points where the front did *not* exhibit an NCFR), 63 points (7.9%) had $p[\text{TN}] > 0.6$. Of these, 15 points exhibited frontolysis (i.e. total $F < 0$). An example of high $p[\text{TN}]$ in a region of frontolysis is shown in Figure 8 for the case of 3 January 2012. In this case, the strong frontolysis is located within the frontal fracture region of a primary cyclone, just off the west coast of Norway⁵ (Figure 8b), where $p[\text{TN}]$ is also very large (> 0.95 ; Figure 8a). A secondary maximum in $p[\text{TN}]$ is evi-

dent further down-front, near a subtle frontal wave over southeast England, where at least one tornado occurred. Since it is unlikely that an NCFR would be present in the frontal fracture region, $p[\text{TN}]$ provides an unrealistic estimate of the true tornado probability in this region. Conversely, near the frontal wave over southeast England, large frontogenesis accompanies large $p[\text{TN}]$, suggesting an NCFR is more likely within this part of the front, and therefore that tornadoes are more likely in this region (as observed).

In order to address this issue, the probability of an NCFR being present, and its dependence on various environmental parameters, was assessed by comparison of the distribution of parameter values at UK and Ireland land points with and without NCFRs. For this purpose, an NCFR was deemed to be present if one could be discerned in composite radar rainfall fields within ~ 100 km of each along-front point, and within ~ 2 hr of the analysis time. The probability of an NCFR was found to be a strong function of total frontogenesis (consistent with the idea that collapse of the frontal zone to small cross-frontal scales, and associated development of an NCFR, requires substantial frontogenesis: e.g. Koch and Kocin, 1991). NCFR probabilities (hereafter $p(\text{NCFR})$) were calculated by dividing the number of points with an NCFR by the total number of points within different frontogenesis classes. The dependence of $p(\text{NCFR})$ on the midpoint frontogenesis for each frontogenesis class may be approximated by the third-order polynomial equation:

$$p(\text{NCFR}) = 0.00004 F^3 - 0.0021F^2 + 0.0467F + 0.4679,$$

where F is the total frontogenesis. Negative values of $p(\text{NCFR})$ are set to zero. This equation was used to derive $p(\text{NCFR})$ for all points in the 3 January 2012 case (Figure 8c). As expected, $p(\text{NCFR})$ is at or close to zero in the frontal fracture region due to the strong frontolysis, but much larger (> 0.7) near the frontal wave over southeast England. Weighting of $p[\text{TN}]$ by $p(\text{NCFR})$, for example by calculating the product of the two parameters, provides a more realistic estimate of tornado risk in this case (Figure 8d), usefully highlighting the region over southern England whilst giving much lower probabilities within the frontal fracture region.

Other non-tornadic points with low $p[\text{TN}]$, where an NCFR was present and frontogenesis was positive, represent situations apparently favourable for tornadoes, but in which no tornadoes were reported. One possible explanation is under-reporting, which is known to be a universal problem with existing tornado databases, being

⁵In this case, these latter analysis points would not have appeared in the filtered dataset in e.g. Figure 3a, since they are not located over UK and

Ireland land areas. However, we choose to discuss the case here because it is a good illustration of the point in hand.

particularly relevant in the case of weaker tornadoes (e.g. Feuerstein *et al.*, 2005). Alternatively, it is possible that the tornadic phase of the event in these cases occurred prior to arrival of the front into the UK and Ireland (recalling that the tornadic period tends to occur relatively early in the life cycle of frontal waves, and that high $p[\text{TN}]$ may persist beyond the tornadic phase). A third possible explanation is provided by analysis of the trends in parameter values. In at least three cases, the wind field showed marked weakening by the next analysis time, suggesting that, where present, the frontal wave was weakening, that the front was moving into a region of weaker large-scale flow, or that the frontal trough was becoming shallower, such that shear vorticity and $-v'_{\text{cold}}$ trends were negative. This is consistent with the results presented in Appendix B, that is, that the presence of a frontal wave is not a sufficient condition for tornadogenesis; non-developmental or weakening waves tend not to favour tornadoes, since they do not exhibit the requisite temporal changes in key parameter values. A final possible explanation for such events was uncovered by operational trials of $p[\text{TN}]$ during winter 2019–2020 (Matthew Lehnert, personal communication, 2020). In one event, the frontal zone was found to comprise multiple shear zones separated by ~ 10 – 20 km in the cross-front direction. Although high-resolution operational models indicated collapse to a single shear zone as the front crossed the UK, in the event this did not occur until after the front had cleared the region. Therefore, although the bulk shear vorticity was large, it continued to be distributed across multiple, weaker shear zones. Such events are likely under-represented in the analysed dataset because they tend to exhibit rather weak and discontinuous NCFRs. The failure to collapse to a single shear zone suggests weak frontogenesis, again highlighting the likely importance of sufficient frontogenesis, in combination with high $p[\text{TN}]$, in tornadic events.

APPENDIX B

Frontal waves in non-tornadic events

Although frontal waves are capable of creating an environment favourable for NCFR tornadoes, as discussed in Section 3.7, a substantial number of non-tornadic cases also exhibited frontal waves at the time of frontal passage across the UK and Ireland. Inspection of surface analysis charts shows that non-tornadic fronts exhibited a warm-front-cold-front pair or an inflection point over or close to the UK in 25 cases (i.e. 36.8% of non-tornadic events; cf. 42.3% of tornadic events and 72.2% of high-tornadic events). In other words, the presence of a frontal wave is not a sufficient condition for tornadogenesis. In order to assess whether tornadic

waves can be distinguished from non-tornadic waves, bulk parameters were compared for frontal wave cases in the high-tornadic, tornadic and non-tornadic event classes. Tornadic and high-tornadic events were treated as one combined class (“all-tornadic”), owing to the relatively small sample size in each individual class. Results show significant differences (at the 95% level) between all-tornadic and non-tornadic waves for several parameters including $-v'_{\text{cold}}$, front-normal forward motion, shear vorticity, total frontogenesis and overall mean wind speed, with tornadic waves having larger median values in each case. Crucially, the median $-v'_{\text{cold}}$ trend was negative for the non-tornadic waves (median value $-0.45 \text{ m}\cdot\text{s}^{-1} / 6 \text{ hr}$) but positive for tornadic events (median value $1.28 \text{ m}\cdot\text{s}^{-1} / 6 \text{ hr}$). Similarly, the shear vorticity trend was near zero in non-tornadic waves (median value $0.3 \times 10^{-5} \text{ s}^{-1} / 6 \text{ hr}$), but positive in tornadic waves (median value $1.39 \times 10^{-5} \text{ s}^{-1} / 6 \text{ hr}$). These results suggest that actively developing waves are more conducive to tornadogenesis than non-developmental waves, and further emphasise the importance of temporal trends in parameter values (i.e. increases in shear vorticity and $-v'_{\text{cold}}$) in tornadic cases.

APPENDIX C

Idealised wind and pressure fields near a frontal wave

As discussed in Section 4.1, the along-front variability in shear vorticity, $-v'_{\text{cold}}$ and $p[\text{TN}]$ arising near to a frontal wave may be understood, in part, by consideration of an idealised “toy model” of the pressure and associated geostrophic wind field, comprising three components:

1. A large-scale background pressure field and associated geostrophic wind field, in which a uniform pressure gradient of $1.18 \times 10^{-5} \text{ hPa}\cdot\text{m}^{-1}$ and associated south-westerly geostrophic flow of $7.9 \text{ m}\cdot\text{s}^{-1}$ are orientated at an angle of 45° to the trailing front, with lower pressure towards the northwest.
2. An S-shaped front and associated pressure trough, the trough having half-width $W = 300 \text{ km}$, with uniform (along the front) central pressure deficit $p_{\text{tr}} = 2 \text{ hPa}$ at the trough axis (collocated with the front), and in which the pressure deficit reduces with increasing distance, w , from the trough axis and front according to $p_{\text{tr}} \left\{ 1 - \sin \left[0.5 \pi \left(\frac{w}{W} \right) \right] \right\}$. Smoothing is applied near the trough axis to avoid very large wind gradients.
3. A circularly symmetric, negative pressure anomaly and associated non-divergent, cyclonic, flow field representing the wave depression pressure and associated geostrophic wind fields. The anomaly central pressure deficit, M , is equal to 4.15 hPa and the pressure deficit

reduces with distance, d , from the centre according to $0.5 M \left\{ 1 - \sin \left[\pi \left(\frac{d}{R} - 0.5 \right) \right] \right\}$, where R is the anomaly radius (600 km).

Superimposing these pressure and wind components yields an idealised depiction of the flow fields near a

frontal wave in the early stages of development. The associated along-front variability in trough structure, shear vorticity and $-v'_{\text{cold}}$ is shown in Figure 13, as described in the main text.